Contents lists available at ScienceDirect

Coordination Chemistry Reviews

journal homepage: www.elsevier.com/locate/ccr

Review

Conductive properties of triphenylene MOFs and COFs

Noemí Contreras-Pereda [a], Salvador Pané [b], Josep Puigmartí-Luis [c,d], Daniel Ruiz-Molina [a,*]

[a] Catalan Institute of Nanoscience and Nanotechnology (ICN2), CSIC and BIST, Campus UAB, Bellaterra, 08193 Barcelona, Spain
[b] Multi-Scale Robotics Lab, ETH Zurich, Tannenstrasse 3, Zurich, CH-8092 Switzerland
[c] Departament de Ciència dels Materials i Química Física, Institut de Química Teòrica i Computacional, 08028 Barcelona, Spain
[d] ICREA, Pg. Lluís Companys 23, 08010 Barcelona, Spain

ARTICLE INFO

ABSTRACT

Triphenylene (TP) based materials have experienced a great expansion in the latest years. TP molecules have interesting optoelectronic properties, arising from the aromatic core, which have been exploited in functional two-dimensional (2D) Metal-Organic Frameworks (MOFs) and Covalent Organic Frameworks (COFs) aside other organic polymers. In this review we summarize synthetic approaches of TP-based 2D MOFs and COFs emphasizing on the resulting morphology, crystalline domains and orientation, proven to have great impact on the properties and performance of these materials in functional devices. Specifically, we report a detailed description on the different TP-based 2D structures detailing the influence of the chemical and crystalline structure on the electronic properties, specially the *in-plane* and *out-of-plane* contribution to the electrical conductivity. Finally, we give also attention and present several examples of functional devices made out with these electronic materials with great impact in the literature as well as in future technological applications.

Contents

## 1. Molecular characteristics and supramolecular properties

Triphenylene (TP) is a polycyclic aromatic hydrocarbon consisting of four orthofused benzene rings with one central ring surrounded by the other three in an alternate fashion (see Fig. 1a), resulting in a large electron cloud with 18 π delocalized electrons [1]. There exists a wealth of derivatives of triphenylene as function of the groups R_1 and R_2 (see Fig. 1a). For instance, TPs exhibit a supramolecular packing mainly through π-π stacking, further optimized by Van der Waals interactions arising from hexasubstituted long alkyl chains that do not perturbate neither the planarity nor the electronic relocation of the TP core. Precisely, the significant electronic delocalization of the resulting supramolecular structures has made TP derivatives as suitable components for different devices, including sensors for neutral aromatic or cationic guests [2], molecular rotors [1], or in highly stable organic-oxygen cell batteries [3]. However, in this review, we will focus mainly on those where R_1 and R_2 are equal between them, and incorporate –OH (henceforth HHTP), –NH$_2$ (henceforth HATP) or -SH (henceforth THT) groups.

Worth to mention and preceding the description of TP-based MOFs and COFs, TP materials have been significantly applied in the area of discotic liquid crystals (DLCs). DLCs are mesophase supramolecular materials, that in a way similar to other liquid crystals, are formed by the columnar stacking of disk-like moieties (see Fig. 1b) [4,5]. As a consequence of this assembly, DLCs exhibit broad energetic band gaps, where conduction occurs mainly due to hopping of charge carriers rather than a band-like effect, relying on the interplanar distance between TP molecules [6]. Therefore, DLCs often require electrochemical or photochemical doping or charge injection from metallic surfaces moieties for enhanced electronic conductivity [7]. In this case, large electronic delocalization leads to strong charge carrier percolation along the columnar axis, which makes these materials one-dimensional organic semiconductors [5]. For example, the incorporation of nitrogen-doped planar moieties as an electron acceptor generates an intercalated donor–acceptor DLC system with good electrical capacities, and suitable as a cathode in Li batteries [8]. DLCs are also characterized by their easy processability into thin films [4], enabling their integration as components in devices for optoelectronic applications such as organic photovoltaics or organic light-emitting diode (OLEDs) technologies [6].

According with previous considerations, TP-based conductive 1D structures are promising building blocks for advanced optoelectronics. Yet, applications in this domain have been hampered because the lack of reproducibility and required robustness of these architectures. The reason for this is that charge carrier mobility is strongly dependent on the crystallinity of the mesophase [6,9], which varies considerably in DLCs because of the interactions between TP moieties. Alternatively, DLCs can also be obtained with linear and flexible covalent polymers bearing TP moieties that stack into columnar phases, in which the bended side chains are positioned in the outer surface of the column [10]. Though, control over the crystallinity remains strongly dependent on the nature and bendable character of the building blocks used in these investigations [11].

Recent years have seen a wealth of research devoted to the development of TP-based 2D metal–organic frameworks (MOFs) and covalent organic frameworks (COFs) with broad electronic bands for enhanced electronic conduction. COFs and MOFs are polymeric crystalline porous network materials that consist of organic building blocks that polymerize through covalent or coordination bonds, respectively [12–14]. While covalent bonds ensure a larger thermal and pH stability [14,15], the incorporation of metallic ions can add novel optical, magnetic and/or electrical properties [16]. Contrary to DLCs, TP-based organic frameworks (with a defined crystallinity and long-range order) do not rely on weak interactions but on strong covalent and coordination bonds. Hence, they have a stable and robust structure not as much sensitive to external factors such as temperature (Fig. 1c). Moreover, the configuration and dimensionality of the polymer can be predicted by a rational selection of the metal nodes and the organic linkers, giving rise to a wide variety of 2D structures [17]. These planar polymeric layers can further form a 3D supramolecular structure by interlayer interactions such as π-π stacking, hydrogen bonding, Van der Waals forces, or combinations of these.
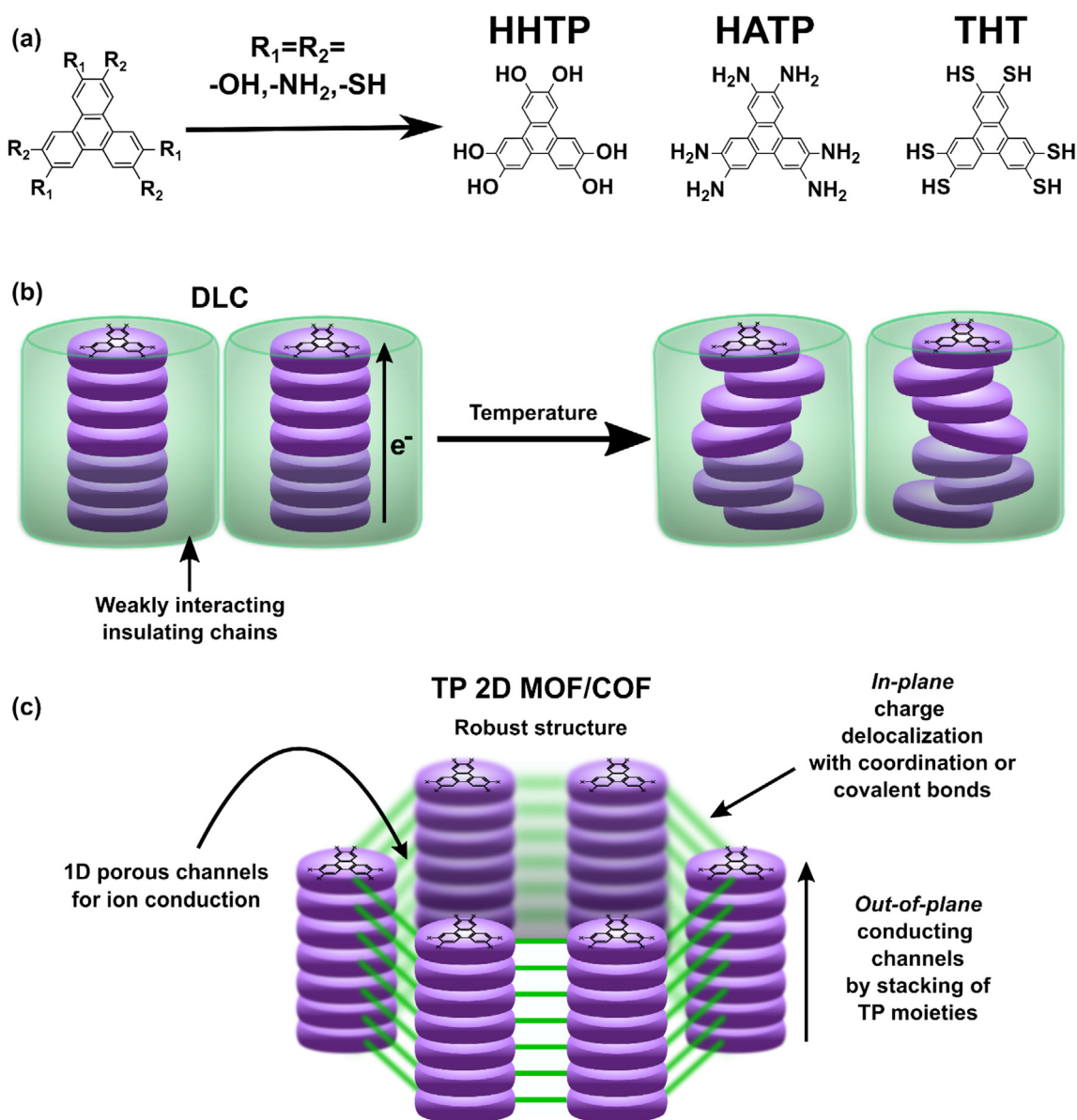
Fig. 1. (a) Chemical structure of a TP molecule. When having identical hexasubstitutions different ligand arise being HHTP for 2,3,6,7,10,11 hexahydroxytriphenylene, HATP for 2,3,6,7,10,11 hexaaminotriphenylene and THT for 2,3,6,7,10,11 triphenylenehexathiol. (b) Schematic of stacking of TP moieties in DLCs forming 1D conducting channels. The supramolecular mesophase structure relies on weak interactions that can be broken upon external stimuli as temperature. (c) Schematic of the stacking of TP moieties in TP-based 2D MOFs and COFs. The crystalline packing ensures a robust structure formed by several hexagonally distributed 1D conducting channels. Furthermore, large *in-plane* delocalization can be obtained along the 2D layers depending on the coordination or covalent bonds used. Moreover, the structure defines 1D pores suitable for host–guest interactions or ionic conduction.

The incorporation of TP moieties in MOFs and COFs is schematically represented in Fig. 2. The 2D layers present a honeycomb graphitic architecture that results in interesting band structures and properties. Regarding the electronic properties, two main components arise: (a) conduction of charge carriers along the 2D layers (*in-plane*) and, (b) interlayer charge transfer (*out-of-plane* conduction) [18]. *In-plane* conduction is usually found for TP-based 2D MOFs where coordination bonds typically lead to large electron delocalization and conjugation pathways along the 2D layers, which results in high *in-plane* conductivities. Strong delocalizations can be a direct consequence of the strong coordination of d-π bonds (normally arising by the rational selection of suitable metallic centers and TP substitution) [19]. Contrarily, covalent bonds formed in TP-based COF structures need to maintain the conjugation in order to lead to such conductivities [20]. TP-based 2D COFs can present a wide variety of π-conjugation depending

on the chemical structure and the condensation bonds forming the 2D layers. Boronate ester condensation leads to COFs with poor conjugation and hence low charge delocalization along the 2D layers [21]. On the other hand, phenazine condensed COFs present a larger conjugation leading to a larger *in-plane* charge transfer. Thus, very few examples of conductive COFs have been reported, which commonly require of either chemical (including donor atoms in their chemical structure) or external doping to aim for electronic applications [14]. *Out-of-plane* conductivities are determined by the supramolecular stacking of the 2D layers. In a similar fashion to DLCs, layer stacking of the TP moieties can lead to one-dimensional charge transfer channels, where charge transfer occurs in through-space pathways [18]. However, different stacking geometries (being mostly eclipsed, nearly-eclipsed or slipped-parallel) can be found, being always governed by the chemical structure of the TP-based 2D MOF/COF under investigation. Hence,
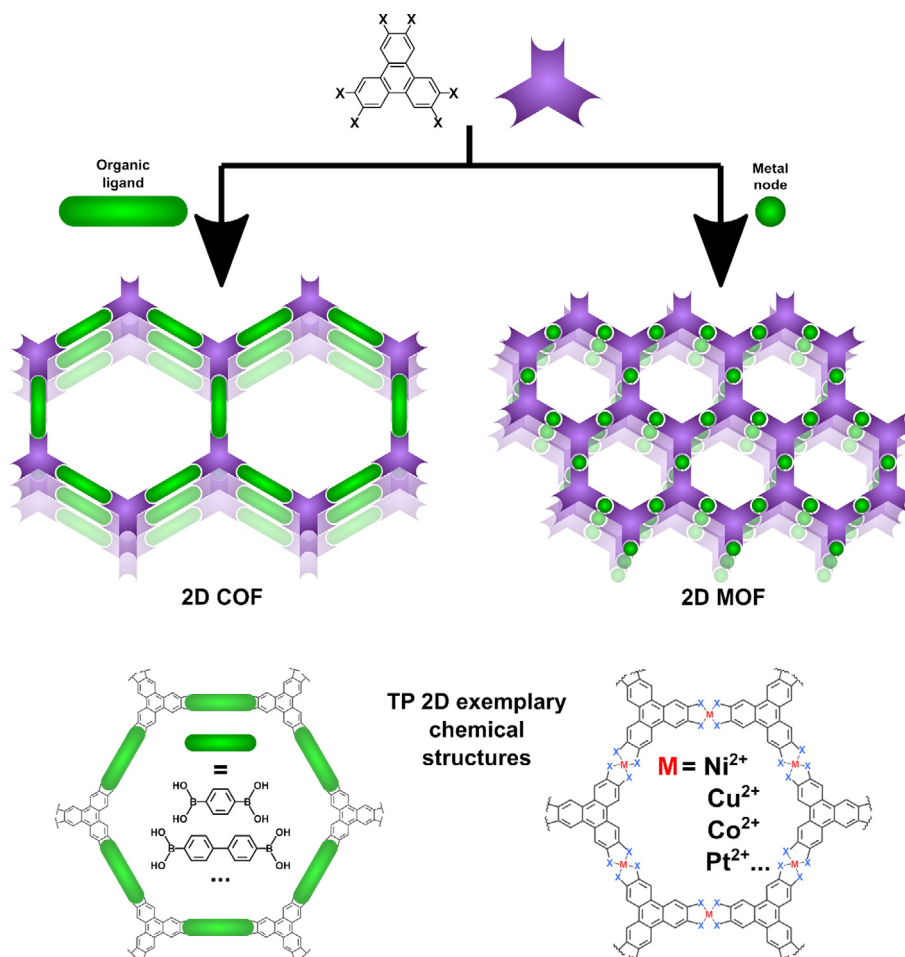
Fig. 2. Scheme of the formation of TP-based 2D MOFs and TP-based 2D COFs. TP 2D MOFs are typically formed by coordination of a metallic ion with the electron donor heteroatoms from TP functionalization. TP 2D COFs are formed by covalently linking TP functional substituents with other organic ligands. The three-fold geometry of TP leads to honeycomb hexagonal structures. Exemplary structures of TP 2D MOFs and COFs layers are shown. In the case of TP 2D MOFs, the planar coordination centers MX_4 defines the honeycomb graphitic structure. On the other hand, in the case of TP 2D COFs, the structure depends on the geometry and the covalent bonding with other organic ligands.

the crystalline structure has a significant impact on the *in-plane* and *out-of-plane* contributions of the optoelectronic properties of TP-based MOFs/COFs. In the following, the impact of the chemical structures of TP-based MOFs/COFs in the final *in-plane* and *out-of-plane* charge transfer properties will be discussed.

2. Synthetic methodologies

Features such as the crystallinity and crystallite size of MOFs and COFs can dramatically impact on their conductive properties [18,22]. To date, control over these parameters has been investigated as function of the methodology used for their synthesis. Accordingly, the methods and synthetic approaches used for the controlled nucleation and growth of these materials has become a very relevant topic in this research area. Most representative examples obtained with different methodologies are discussed in the following sections (see the chemical structures of all the examples in the following Sections 3 and 4).

2.1. Bulk synthesis

2.1.1. Solvothermal reactions
The most common method for the synthesis of TP-based 2D MOFs and COFs is the solvothermal synthesis. In this approach, reactants are dispersed or solubilized in a common solvent and heated up in either a sealed or an opened glassware, depending on the requirement of oxygen in the reaction (see Fig. 3).

TP-based solvothermal reactions of MOFs are characterized by a fast uncontrollable crystallization, leading to several nucleation events in the reaction media. Studies to enhance the crystallinity and particle size were attempted by changing the order of addition or modifying the amount of additives [25,26]. In any case, the largest TP-based 2D MOFs reported with this approach yielded crystals in the order of few micrometers in length being $Cu_3(HHTP)_2$ the main example (Fig. 3c) [24]. In the case of COFs, long reaction times are required to ensure the crystallization of the covalently bonded porous polymeric structure, which are obtained mostly in the form of insoluble powders (Fig. 3b), as first described by Yaghi and co-workers for COF-5 [23]. These reaction mixtures are characterized by their heterogeneity, which causes the occlusion of reagents within the precipitated material and low synthetic yields [27,28]. Thus, studies on homogeneous polymerization have been sought aiming for large crystallization rates and reduced reaction times [28]. For instance, the formation rate dependence of COF-5 with temperature, concentration and presence of additives allowed for the generation of micrometer-long polycrystalline aggregates.

2.1.2. Sonochemical reactions
The reaction between monomers assisted by ultrasound in solution is controlled by tuning parameters such as solvent, sonication
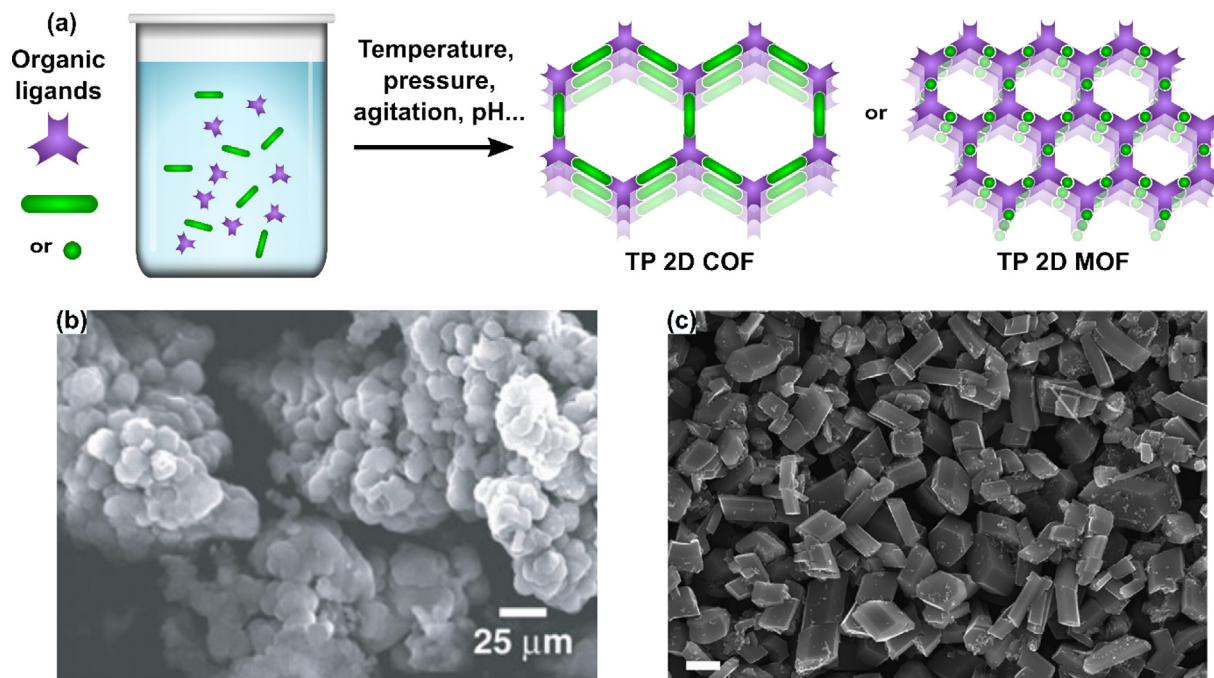
Fig. 3. (a) Scheme illustrating solvothermal reaction syntheses of TP-based 2D MOFs and COFs. (b) Scanning Electron Microscopy (SEM) image of crystals of COF-5 obtained with solvothermal methods. Image reproduced with permission from [23]. (c) SEM image of crystals of $Cu_3(HHTP)_2$ obtained with solvothermal methods. Scale bar is 1 μm. Image reproduced with permission from [24].

Fig. 4. Scheme of the sonochemical reaction of TP-based 2D COFs. (b) and (c) SEM images of crystals of the same COF-5 obtained with sonochemical reactions obtained under different conditions. As observed, small and narrow size distribution of particles is obtained. Images reproduced with permission from [27].

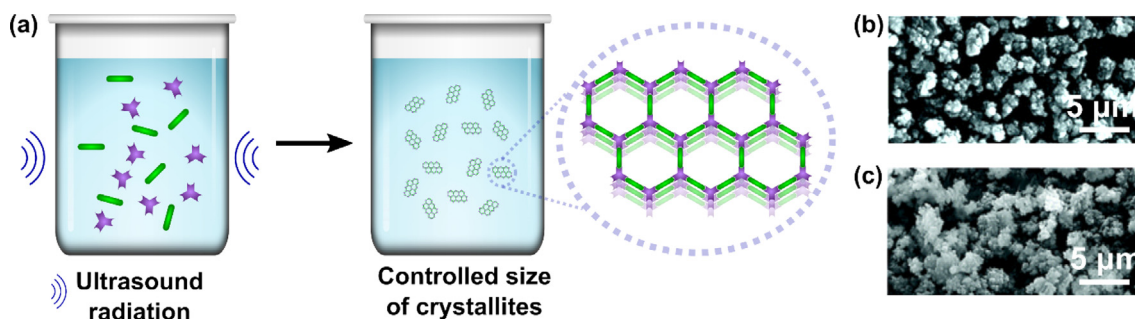times or power. These parameters are changed to modulate the crystallinity, dimensions and porosity of the obtained powders (Fig. 4). Sonochemical syntheses enables faster crystallization, which consequently lowers the reaction times to few hours or even minutes [27]. Moreover, TP-based organic frameworks with larger surface areas than those reported by solvothermal methods can be achieved using this approach. While sonochemical reactions are widely employed for the synthesis of COFs, they are rarely applied in MOF synthesis as small sized crystals are already obtained with solvothermal synthesis.

2.2. Template-assisted syntheses

In recent years, different techniques have been described regarding post-synthetic on-substrate deposition, such as drop-casting of colloidal suspensions of TP-based 2D MOFs (either as-synthetized [29] or after sonication [30]), or TP-based 2D COFs, onto surfaces [31]. Apart from the typical drop-casting approach, other top-down techniques include spin-coating [32], ball-milling blending and abrasion of powders onto substrates [33], or spray-coating of colloidal suspension onto flexible substrates with a high

control on the coverage area and patterning [26]. However, in most of the cases, crystalline powders are not always suitable for device fabrication because they typically form rough interfaces, which lead to charge entrapment and poor ohmic contacts [34]. The incorporation of TP-based MOFs on surfaces can be eased by adding the substrates in the reaction pot (Fig. 5a). A wide variety of suitable substrates for the growth of TP-based MOFs have been described (Fig. 5c) including flat substrates for thin film formation [35] and coating of textiles [36], carbon paper [37], shrinkable flexible substrates [38], core–shell materials [39–41] or metallic meshes [42].

Solvothermal or sonochemical reactions were also used to induce the epitaxial growth of COFs on substrates capitalizing on interactions between the monomers and the immersed substrate (Fig. 5b). As an example, Dichtel et al. grew nanometer-thick COF-5 and Pyr-COF thin films on single layer graphene substrates, which were dipped into the reaction mixture [43]. The highly dense TP-based COF films generated showcased smooth surfaces and long-range order with preferential orientation in the c-axis, independently of the substrate used to support the graphene single layer. Growth of TP-based 2D COFs on a large variety of substrates
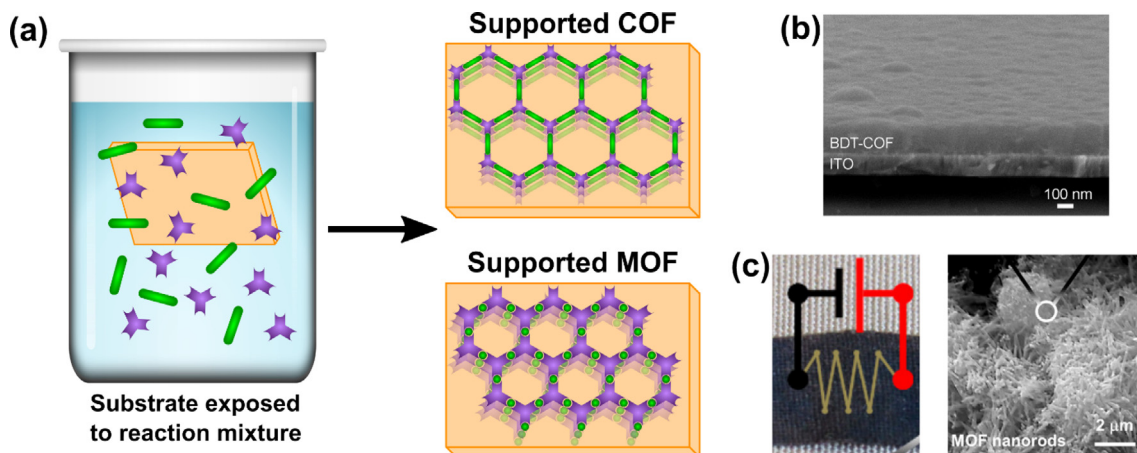
Fig. 5. (a) Schematic of template-assisted synthesis based on the immersion of a substrate in a solvothermal reaction mixture. (b) Cross-section SEM image of a benzothiophene-based COF (BDT-COF) thin film grown on top of a rigid metallic substrate through template-assisted method. Image reproduced with permission from [48]. (c) Picture and SEM image of Ni$_3$(HHTP)$_2$ MOF grown on flexible cotton textile through template-assisted method. Images reproduced with permission from [36].

has also been reported, with carbonaceous architectures such as carbon nanotubes and free standing graphene [44,45]. This technique has also been used to grow COF-5 on the inner surface of polydopamine-coated capillars [46]. The capillary was filled with the reaction mixture, sealed and subjected to high temperature similarly as in a solvothermal approach. Higher quality and scalable thin films can be obtained also by combining a template-assisted method with a colloidal template strategy [47]. During the template-assisted formation of several TP-based 2D COFs (*e.g.*: COF-5, COF-10, Pyr-COF, and DBP-COF), unwanted COF nanoparticles are concomitantly form in the bulk of the solvent upon addition of co-solvents and remain as a stable colloidal suspension. Consequently, irregular deposition of COF particles is

minimized and only heterogeneous nucleation and growth of films with low roughness occurs on the substrate.

2.2.1. Layer-by-Layer (LbL)

This approach has been mainly explored for TP-based 2D MOFs. Typically, substrates are functionalized with active sites to entrap the metal ion on the surface (Fig. 6a). Next, the metal-loaded substrate is exposed to the TP-substituted moiety saturating all the available metallic centers through coordination bonds and leaving coordination sites available. Then, the substrate is exposed again to a metallic solution. This procedure is repeated in a cyclic fashion inducing a homogeneous and layered growth of thin films of large lateral sizes. This approach is characterized by the control over
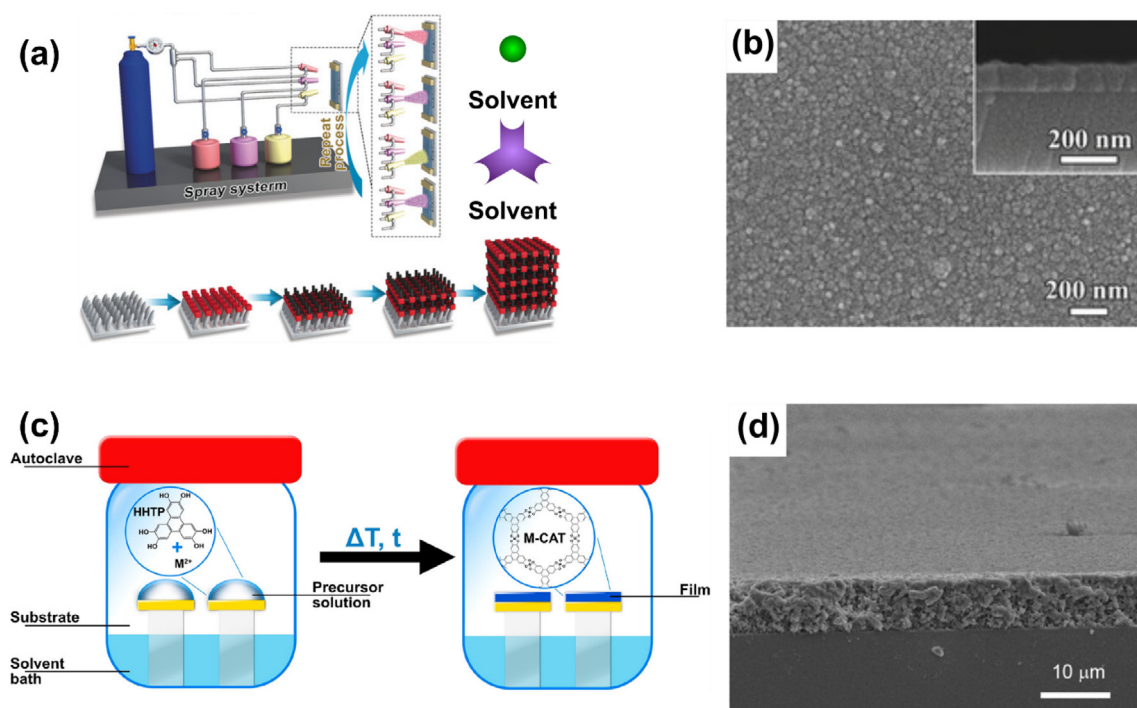
Fig. 6. (a) and (b) Schematic of a layer-by-layer growth of TP-based 2D MOFs using spray-drying of the TP and metallic moieties and SEM image of the obtained Cu$_3$(HHTP)$_2$ MOF with this technique, respectively. Images adapted with permission from [51]. (c) Schematic illustration of the vapor assisted conversion method. Image reproduced with permission from [52]. (d) SEM image of a BDT-COF grown with vapor assisted conversion. Image reproduced with permission from [53].
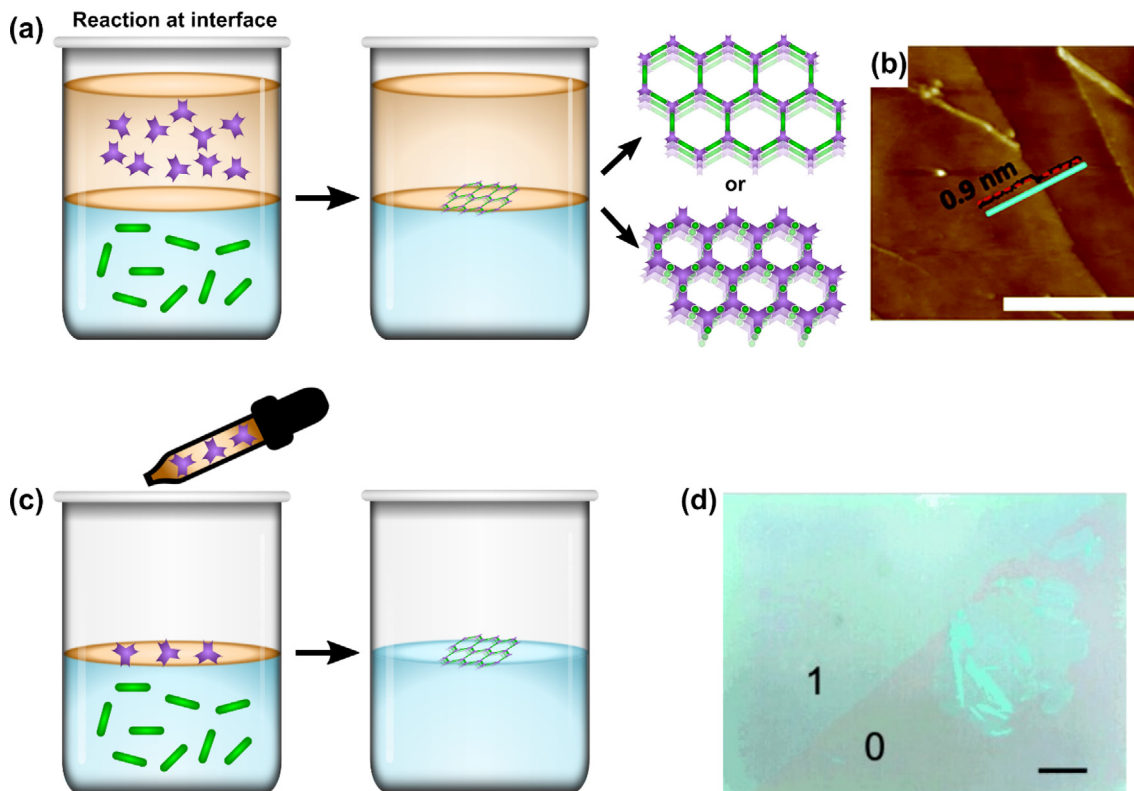
Fig. 7. (a) Illustration showing a liquid–liquid interfacial synthesis. The starting monomers are in different immiscible liquid phases and the reaction between them occurs at the interface. The reaction and growth are mediated by the diffusion of the monomers towards the interface. (b) Atomic Force Microscopy (AFM) image of a TP-based graphdyine COF obtained in a liquid–liquid interface. Image reproduced with permission from [59]. (c) Schematic illustration of a liquid–gas interfacial synthesis. One monomer meets the reaction mixture at the liquid–air interface, it can be added in a gas form. (d) Optical microscopy (OM) image of a $Ni_3(THT)_2$ MOF single-layer thin film grown through liquid–air interface. Image reproduced with permission from [56].

the thickness of the films being generated, and it is directly related to the number of applied cycles. Note that $Cu_3(HHTP)_2$ thin films obtained with LbL methods grow epitaxially having highly oriented crystallites (Fig. 6b). Remarkably, the deposition can be performed with different methods such as substrate immersion in solutions [49,50] or spraying the solutions onto the substrate [51]. The main drawback of LbL approaches is their high time consumption.

2.2.2. Vapor-assisted conversion

This methodology has been recently reported for TP-based 2D MOFs, more specifically for $Ni_9(HHTP)_4$, $Co_9(HHTP)_4$ and $Cu_3(HHTP)_2$ structures [52], and relies on the reaction between starting monomers on a wet surface at the solvent gas pressure conditions (Fig. 6c). This leads to a saturated reaction environment nearby the substrate's surface. This method allowed for growing highly oriented centimeter-long thin films on different substrates both insulating and conducting. However, optimization from substrate to substrate was required. For some specimens, some acidic modulators were needed in the synthesis in order to obtain homogeneous films on the substrates including large coverage. In the case of COFs, the vapor-assisted conversion approach was introduced by Bein and co-workers in 2015 as a scalable method for the production of thin films of COF-5 and BDT-COF. Specially, the approach allows for the formation of COF thin films at room temperature with a high control on their thicknesses ranging from hundred nanometers to the micrometer scale (Fig. 6d) [53].

2.3. Interfacial syntheses of thin films

In the case of TP-based 2D MOF syntheses using liquid–liquid interfaces, the metallic salt and the organic ligand are dissolved in different immiscible solvents, thus confining the reaction at the interface upon the slow diffusion of the reactants (Fig. 7a and c) [54,55]. By means of this approach, thin films with sub-millimeter lateral sizes can be obtained. Yet, the fabrication of films with nanometer thicknesses still remains a challenge due to the lack of homogeneity along the film [54]. One of the most representative approaches used at liquid–gas interface is certainly the Langmuir-Blodget technique, resulting in the growth of sub-millimeter films with nanoscale thicknesses. Main achievements are the growth of a 2D monolayer of $Ni_3(THT)_2$ MOF [56] or $Cu_3(HHTP)_2$ MOF thin films with high preferential orientation [54] (Fig. 7d). Note that by using this controlled growth and a stamping approach in a repeated fashion, one can achieve a controlled increase of the film thickness [54]. Another approach is the use of reagents in gas phase such as ammonia vapors [57] or atmospheric oxygen (as reported for the growth of $Ni_3(HITP)_2$) [58]. The thin film formed at the interface grows upon diffusion of the gases into the liquid phase. Hence, control on the thickness is achieved upon the control of the reaction time. Importantly, this approach can generate films with lateral dimensions of hundreds of microns, which lead to specimens with lower conductivities than those previously reported for compressed pellets. Moreover, the obtained thin films were polycrystalline and randomly orientated. Interfacial syntheses have been largely exploited for TP-based MOFs whereas regarding TP-based COF structures, synthesis of TP-based graphdyine using Glaser-Hay cross-coupling reactions is the only example of interfacial synthesis reported to date. In this case, the starting monomer is in one phase and the copper catalyzer in the other leading to thin films with sub-nanometer thicknesses (Fig. 7b) [59].
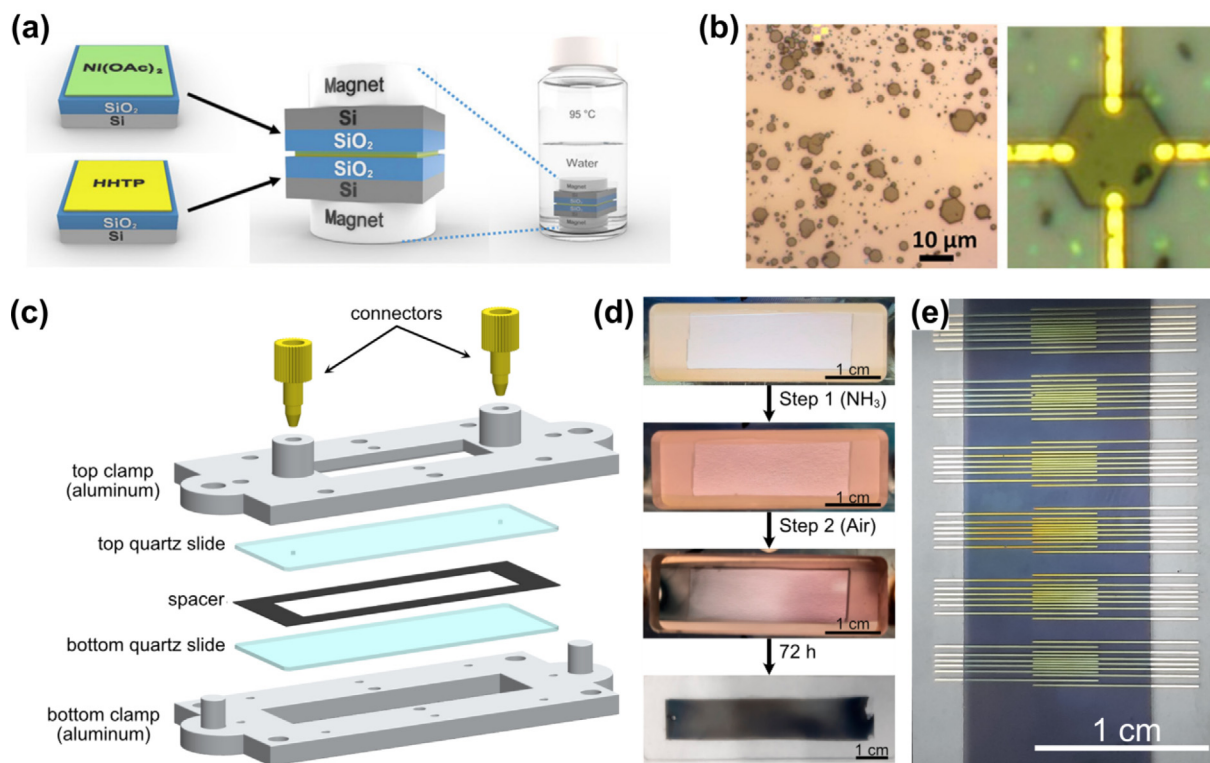
Fig. 8. (a) Schematic illustration of the synthesis of TP-based 2D MOF between pressed substrates. The two substrates, each containing a starting monomer, are pressed together and exposed to the solvent. The reaction takes place between the substrates when the solvent is incorporated via capillary forces. (b) OM images of the $Ni_3(HHTP)_2$ MOF crystals obtained with pressed substrates system. Images reproduced with permission from [60]. (c) Illustration of the microfluidic devices designed to simulate microgravity conditions. Two substrates are clamped together with a spacer in between. The space left between the two substrates by the spacer define the microfluidic environment used for the synthesis. (d) Optical images of the different reaction stages achieved during the synthesis of $Ni_3(HITP)_2$ inside the microfluidic device. (e) Micrograph of the obtained $Ni_3(HITP)_2$ thin film using a simulated microgravity environment. Images reproduced with permission from [63].

2.4. Microfludic devices

2.4.1. Pressed substrates

Recent approaches based on mimicking capillary forces have enabled control on the crystallization of TP-based 2D MOFs [60,61]. In one example reported by Dincă and co-workers, synthesis of $Ni_9(HHTP)_4$ crystals occurs between two silicon substrates. The flat surfaces are placed face-to-face and pressed one against the other with two attracting magnets. In this system, the organic ligand and the metallic ion are previously deposited on either substrates (HHTP needs to be deposited through ultra-high vacuum (UHV) thermal evaporation for a planar deposition on the surface) [60]. Later, the two pressed substrates are immersed in the reaction solvent and heated as shown in Fig. 8a. The confinement occurring between the two substrates enhances the MOF growth perpendicularly to the c-axis (favoring the metal–organic bond coordination over the stacking of layers). This has enabled the formation of hexagonal plate-like crystals with lateral sizes of 1–10 μm (in sharp contrast to the needle-like crystals typically obtained in *in situ* reactions) (Fig. 8b). Alternatively, in another example, the pressed substrates were be previously functionalized with hydroxyl groups using a piranha solution (or UV-ozone treatment) and were subjected to a layer-by-layer growth [61]. Centimeter-scale $Ni_9(HHTP)_4$, $Co_9(HHTP)_4$ and $Cu_3(HHTP)_2$ thin films with very controlled thicknesses were obtained on top of commercial silicon wafers with a preferential orientation.

2.4.2. Continuous flow

Less explored methods to obtain TP-based 2D COFs have been occasionally reported [14]. This is the case of COF-5, COF-10,

Pyr-COF and DBP-COF thin films grown under continuous flow conditions [62]. In a recent contribution reported by Dichtel and co-workers, monomers solutions are pumped and passed over a substrate under heating conditions. The continuous flow prevents the irregular deposition of COF colloids formed in solution on the substrate. The technique is characterized by a constant rate growth, allowing for a high control on the thickness of the thin film. Studies on the crystallinity of the generated thin films confirmed that growth relies not only on the flow of the monomeric species over the substrate but also on the pre-polymerized oligomers obtained from flowed solutions.

2.4.3. Simulated microgravity environment

Our groups have recently reported a novel microfluidic device preventing the presence of convection flows simulating thus the effect of microgravity on Earth [63]. The engineered device is made of two sandwiched substrates that are spaced by a micrometer-thick silicone film (Fig. 8c). Centimeter-large films of $Ni_3(HITP)_2$ MOFs with nanoscale thicknesses on both insulating and conducting substrates were obtained with this method with a large control on their preferential orientation (obtaining both c-axis and ab-axis oriented films) which allowed to assess the anisotropy in the electronic conduction (Fig. 8d and e).

2.5. On-surface UHV evaporation

The UHV evaporation of TP-based monomers on metallic surfaces has provided new insights information on the synthesis of supported TP-based 2D MOF/COF layers [64,65]. Note that TP molecules are planarly adsorbed on the surface in organized and

oriented domains. The geometry of the packaging is determined by the supramolecular interaction between TP molecules, typically repulsive and leading to two closed-packed orientations rotated 60° respect to each other [64]. Interestingly, the introduction of functional groups (such as hydroxyl groups) has great impact on the available packing geometries. Depending on the evaporation conditions, strong interactions between introduced functional groups can come into play and direct the growth of typical honeycomb structures of TP-based 2D MOFs and COFs [65]. The success of these studies prompted the synthesis of TP-based 2D MOF monolayers by the sequential evaporation of the TP-based ligand and a metallic center (see Fig. 9a). Remarkably, the direct evaporation of HATP molecules onto surfaces containing possible coordination centers (*e.g.*, copper substrates) did not lead to an extended coordination but to discrete coordination clusters. Thus, after the thermal evaporation of the TP molecule, co-deposition of a Ni metallic center with electron beam evaporation and annealing are required to obtain unit cells of TP-based 2D MOF $Ni_3(HITP)_2$ monolayers (Fig. 9c). This research culminated in a more robust protocol, where the thermal evaporation of HATP is sequentially followed by the evaporation of the metallic cluster enabling the growth of single-layer structures of $Ni_3(HITP)_2$ [66] and $Fe_3(HITP)_2$ [67].

Supported monolayered domains of TP-based 2D COFs could also be obtained by thermal evaporation of the starting organic monomers in UHV and deposition on metallic surfaces [69]. Catalyzed by the substrate and upon annealing treatment, covalent bonds between the deposited monomers occur, generating the expected porous organized network (Fig. 9b). This approach leads to the formation of atom-thick molecular films, which are very useful for fundamental studies, though still far from practical applications.

3. Triphenylene-based 2D MOFs

In the following, we will review different examples of TP-based MOFs described to date with special attention to the chemical families and conductive properties.

3.1. Chemical families

TP ligands coordinate with either square planar or octahedral metal ions with unavailable axial positions, such as Ni^{2+}, Co^{2+} or Cu^{2+}, to keep the planar coordination along the 2D layers [70].

The resulting honeycomb graphitic structures exhibit an hexagonal porous structure that displays a large electron delocalization, which leads to high *in-plane* conductivities along the 2D coordinated layer [19]. The radius of the donor atom in the TP moiety and the electronic configuration of the metallic ion have great impact on the π-d orbital hybridization of the material, as it determines the bond distance and the strength of the MX_4 moieties [19]. Accordingly, the electronic conductivity can be tailored by using different combination of TP substitutions and metallic centers [22]. These features are key factors to ensure the *in-plane* charge conduction. For instance, TP-based MOFs incorporating MO_4 moieties typically showcase lower charge transport than the homologous TP-based MOFs comprising MN_4 moieties. Moreover, the Kagomé lattice arrangement of the metallic centers may originate band structures with the presence of Dirac points, where ultrafast charge carrier mobilities and non-trivial physical properties as topological states can arise [19,71]. Additionally, TP can be oxidized during the MOF formation reaching up to a total charge of −3, some of the intermediate species being stable radicals [71]. Concerning the *out-of-plane* contribution to conductivity, different stacking of the layers and crystalline arrangements can modify the MOF bulk physical properties and the electron conduction arising from differences in the overlap of the TP moieties within the structure. Further, extended 1D pore channels arise in the case of an eclipsed or nearly-eclipsed stacking of the layers that can be used to modify the properties through interaction with analytes or doping encapsulation [70]. Next, a summary of different TP-based 2D MOFs reported and their corresponding conductivity properties are grouped as function of the used donor heteroatom.

3.1.1. HHTP-based 2D MOFs

In 2012, Yaghi and co-workers reported the first TP-based 2D MOF using HHTP and Ni^{2+}, Co^{2+} and Cu^{2+} as metal ions [72]. X-ray diffraction (XRD) of the Co-based MOF revealed extended layered honeycomb networks combining cobalt ions and HHTP molecules (Fig. 10a and b). The metallic center showcased octahedral geometries with two terminal water ligands in the axial positions and the HHTP molecules in equatorial positions. These 2D coordination layers pile up by the π-π stacking of the triphenylene units in an alternated ABAB stacking pattern, leading to a 3D supramolecular structure. Additionally, the coordination layers are intercalated with layers of molecules with formula [(H2O)4-Co]3HHTP. Hence, the final formula of the Co-based MOF resulted in $Co_9(HHTP)_4$ excluding the coordinated water molecules. On
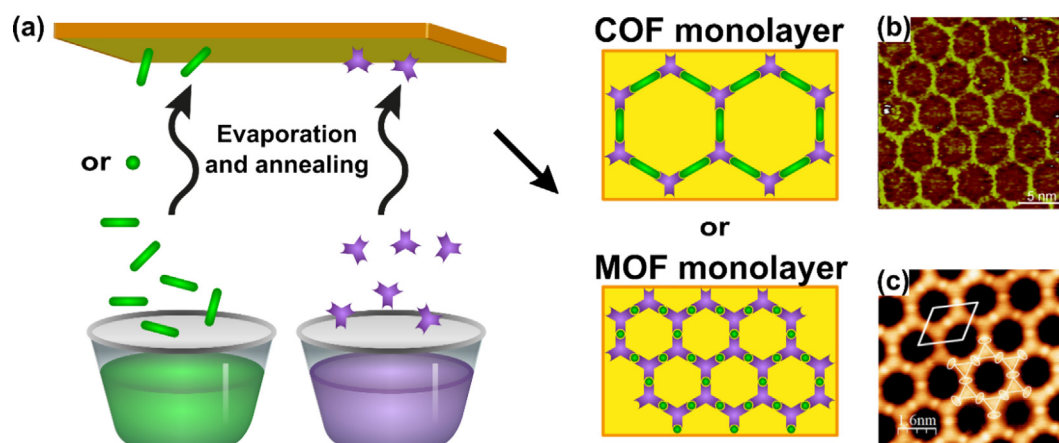
Fig. 9. (a) Schematic of the UHV evaporation synthesis. The monomers are evaporated onto a substrate which will catalyze their reaction to form COF or MOF monolayers. (b) and (c) Scanning Tunneling Microscopy of COF-10 and $Fe_3(HITP)_2$ MOF monolayers, respectively. Both materials showcase the characteristic honeycomb porous structure expected for these materials. Images reproduced with permission from [68 and 67], respectively.
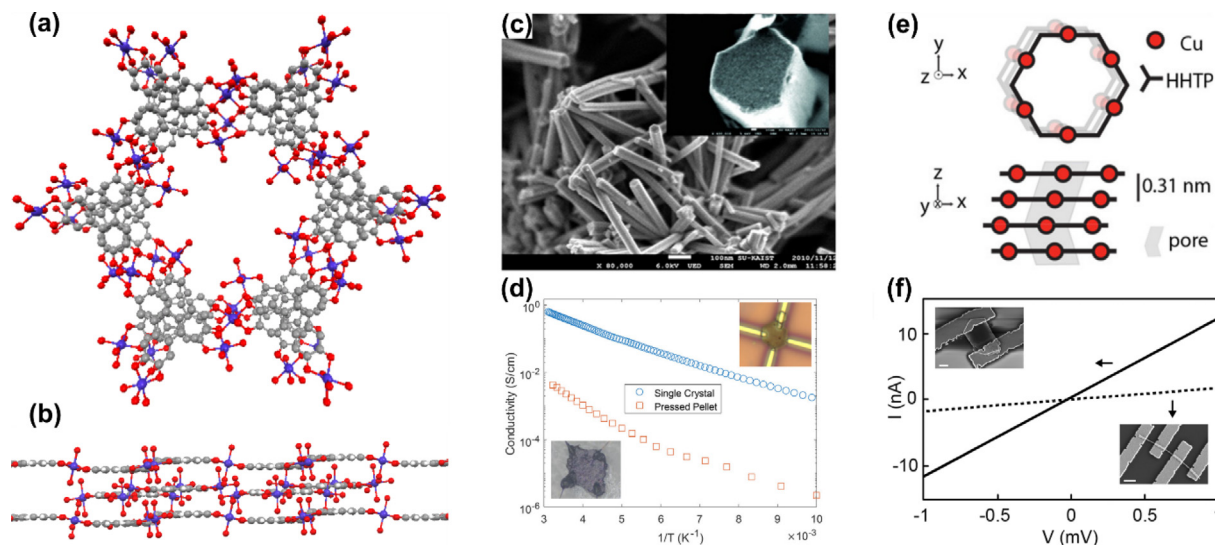
Fig. 10. (a) and (b) Top and side view of the 2D layers in the Co$_9$(HHTP)$_4$ structure, respectively. In (b), the discrete molecular units (*i.e.* [(H$_2$O)$_4$Co]$_3$HHTP) can be easily appreciated between the layers showing the distortion that they generate to the π-π stacking of the TP moieties in an eclipsed orientation. (c) SEM images of rod-like Ni$_9$(HHTP)$_4$ crystals. Image reproduced with permission from [72]. (d) Temperature dependence of the electrical conductivity of a Ni$_9$(HHTP)$_4$ single crystal and of a corresponding pressed pellet. Defects arising from polycrystalline pressed pellets led to lower conductivities and different temperature dependance when compared to single crystal devices. Insets: optical microscope images of a single-crystal and a pressed-pellet devices. Image reproduced with permission from [60]. (e) Schematic illustration of the structure of Cu$_3$(HHTP)$_2$ crystals. The structure is characterized by a continuous shifting of the layers. (f) I-V curves of plate-like (full line) and rod-like (dashed line) Cu$_3$(HHTP)$_2$ crystals taken at room temperature, respectively. Each shape allowed to assess the *in-plane* and *out-of-plane* contributions to electrical conductivity. Images reproduced with permission from [24].

the other hand, the hexagonal rod-like Ni-based MOF resulted isostructural to the Co-based MOF according to powder XRD and high-resolution transmission electron microscopy (HR-TEM) images (Fig. 10c). Conductivity measurements of M$_9$(HTTP)$_4$ (M = Co and Ni) pressed pellets showed low conductivities in the order of 10^{-3} S·cm^{-1} as the discrete molecular coordination units are interlocked between the layers, decreasing the charge interlayer delocalization [72]. Recently, in their seminal contribution, Dincă and co-workers grew single crystals of Ni$_9$(HTTP)$_4$, to allow for measurements *in-plane* conductivity (0.4 S·cm^{-1}) and *out-of-plane* conductivities (10^{-4} S·cm^{-1}) (Fig. 10d) [60]. The remarkable difference of up to three orders of magnitude between *in-plane* and *out-of-plane* conductivities highlights the relevant charge transport mediated by the conjugated TP-based 2D MOF layers. Clearly, and based on these results, one can conclude that the interlayer charge transport in these MOFs hardly contributes to the conductivity. This effect probably results from the large distance between the layers and their disordered stacking.

Interestingly, the powder XRD pattern of the Cu-based MOF indicated the presence of a different crystalline phase, as confirmed afterwards by Dincă and co-workers using powder XRD and HR-TEM. In this case, the layers are stacked in an almost eclipsed fashion (Fig. 10e), with a slight continuous shift along the *ab*-direction, without any occlusion of molecular coordination units, and an expected formula of Cu$_3$(HHTP)$_2$ [24]. Yaghi *et al.* showed that Cu$_3$(HHTP)$_2$ single crystals could led to conductivity values as high as 0.1 S cm^{-1} [72]. Later, Dincă and co-workers confirmed this value by measuring the conductivity of Cu$_3$(HHTP)$_2$ plate-like crystals with their 2D layers oriented along the crystal plane. In this case, the Cu$_3$(HHTP)$_2$ plate-like crystals were synthetized using a sonication-assisted synthesis (Fig. 10f) [24]. *In-plane* and *out-of-plane* conductivities of the 2D layers were 0.5 S·cm^{-1} and 1.5 S·cm^{-1}, respectively, confirming equal contribution of intralayer and interlayer charge transport (arising from the large planar conjugation and eclipsed stacking of the TP molecules). As expected, polycrystalline Cu$_3$(HHTP)$_2$ samples provided conductivities in the range of 10^{-1}–10^{-3} S·cm^{-1}. This variation depends on the synthetic method, which affects the morphology,

and hence, the charge transport properties. Table 1 summarizes the conductivities of HHTP-based TP-based 2D MOFs showing the impact of the measured morphologies and crystalline orientations.

The influence of the stacking interaction between the TP moieties in the conductivity properties were assessed by investigating a series of lanthanide Ln$_{x+1}$(HHTP) MOFs [73]. In the described structures, Ln centers (Ln = La^{3+}, Nd^{3+}, Ho^{3+}, Yb^{3+}) coordinate to HHTP molecules forming a 3D coordination network, where HHTP molecules are located along 2D planes and Ln centers in between layers. Stacking between HHTP moieties remain close to graphitic π-π interactions having interlayer distances of ~3 Å. Particularly, the use of larger lanthanide ions led to larger interlayer distances, which could be directly correlated to a decrease in the conductivity. Finally, essays on crystallization of TP-based 2D MOFs incorporating Fe ions were firstly attempted by Mirica and co-workers [33]. Despite the lack of crystallinity of the material, the obtained Fe-based material displayed similar conductivities than other pressed pellets of crystalline HHTP-based MOFs, of the order of 10^{-3} S·cm^{-1}. It was only recently that Medina *et al.* reported the successful crystallization of HHTP-based MOFs using Fe ions with similar conductivities [74]. Interestingly, the obtained structures were three-dimensional instead of layered, characterized by supramolecular tetrahedra of four triphenylene units coordinated to a trinuclear iron cluster. Other three-dimensional structures using HHTP as organic ligand have been reported by Yaghi and co-workers that resulted in Fe, Ti and V-based porous anionic frameworks with large proton conductivity [75]. The Fe-based MOF characterized by dimetallic centers, showcased a proton conductivity of 5.0·10^{-2} S·cm^{-1} under 98% of relative humidity at 25 °C. This was attributed to the presence of both sulfate and dimethylammonium (DMA) ions, which combination has great impact on the proton charge transfer. Consequently, the Ti-based MOF with provided lower conductivities of 8.2·10^{-4} S·cm^{-1} under the same conditions since this structure contains only DMA ions.

3.1.2. HATP-based 2D MOFs

One of the first imino-substituted TP-based MOFs reported was Ni$_3$(HITP)$_2$ by Dincă and co-workers in 2014 [35]. The 2D coordina-

Table 1
Conductivities of HHTP-based MOFs.

MOF	Measuring technique	Conditions	Conductivity (S·cm^{-1})	Orientation	Ref
Ni$_9$(HHTP)$_4$	Single crystal (4-probe)	Vacuum	0.4	*ab*-axis	[60]
	Single crystal (2-probe)	Vacuum	$1 \cdot 10^{-4}$	*c*-axis	[60]
	Thin film (vdP)	–	$1.1 \cdot 10^{-3}$	*ab*-axis	[52]
	Pellet (4-probe)	Vacuum	$3.6 \cdot 10^{-3}$	Random	[60]
	Pellet (4-probe)	–	$1 \cdot 10^{-1}$	Random	[33]
	Pellet (4-probe)	–	$1 \cdot 10^{-2}$	Random	[38]
	Pellet (4-probe)	–	0.26	Random	[76]
	Pellet (2-probe)	–	$6.0 \cdot 10^{-3}$	Random	[77]
	Pellet (vdP)	–	$6.8 \cdot 10^{-3}$	Random	[52]
Cu$_3$(HHTP)$_2$	Single crystal (4-probe)	Vacuum	0.2	*c*-axis	[72]
	Single crystal (4-probe)	Vacuum	1.5	*ab*-axis	[24]
	Single crystal (2-probe)	Vacuum	0.5	*c*-axis	[24]
	Film (4-probe)	Vacuum	0.29	*ab*-axis	[49]
	Film (4-probe)	Vacuum	10^{-4}	*ab*-axis	[54]
	Film (4-probe)	Argon	$2.3 \cdot 10^{-2}$	*ab*-axis	[26]
	Film (2-probe)	–	$2 \cdot 10^{-2}$	*ab*-axis	[51]
	Pellet (4-probe)	Argon	$4.5 \cdot 10^{-2}$	Random	[26]
	Pellet (4-probe)	–	$2.0 \cdot 10^{-2}$	Random	[33]
	Pellet (4-probe)	–	$7.6 \cdot 10^{-3}$	Random	[38]
	Pellet (4-probe)	–	$8.0 \cdot 10^{-3}$	Random	[78]
	Pellet (2-probe)	–	$1.0 \cdot 10^{-2}$	Random	[79]
	Pellet (2-probe)	–	$3.0 \cdot 10^{-3}$	Random	[37]
	Pellet (vdP)	–	$2.7 \cdot 10^{-2}$	Random	[52]
Co$_9$(HHTP)$_4$	Thin film (vdP)	–	$3.3 \cdot 10^{-3}$	*ab*-axis	[52]
	Pellet (vdP)	–	$3.2 \cdot 10^{-2}$	Random	[52]
	Pellet (4-probe)	–	$2.7 \cdot 10^{-6}$	Random	[33]
	Pellet (2-probe)	–	$2.0 \cdot 10^{-3}$	Random	[77]
Fe$_3$(HHTP)$_2$	Pellet (4-probe)	Amorphous	$3.0 \cdot 10^{-3}$	Random	[33]
	Pellet (vdP)	Ambient	$5.6 \cdot 10^{-3}$	Random	[74]
Zn$_3$(HHTP)$_2$	Pellet (4-probe)	Amorphous	$5.7 \cdot 10^{-6}$	Random	[78]

tion layers display a honeycomb network with a slipped-parallel structure with a minimal offset direction (see Fig. 11a and b). Accordingly, an almost eclipsed stacking of TP moieties is obtained, converging to large charge delocalization along the material. The resulting conductivities were as high as 40 S·cm^{-1} in polycrystalline thin films, even when grain boundaries dramati-

cally limits the percolation of charge carriers between crystallites [35,70]. A linear increase of the conductivity with the temperature indicated a semiconducting behavior of the material, sustained by the oxidation of the amines into iminosemiquinones and the formation of a hole rich p-type semiconductor. Controversial results were obtained in a more recent study by Day *et al.* on
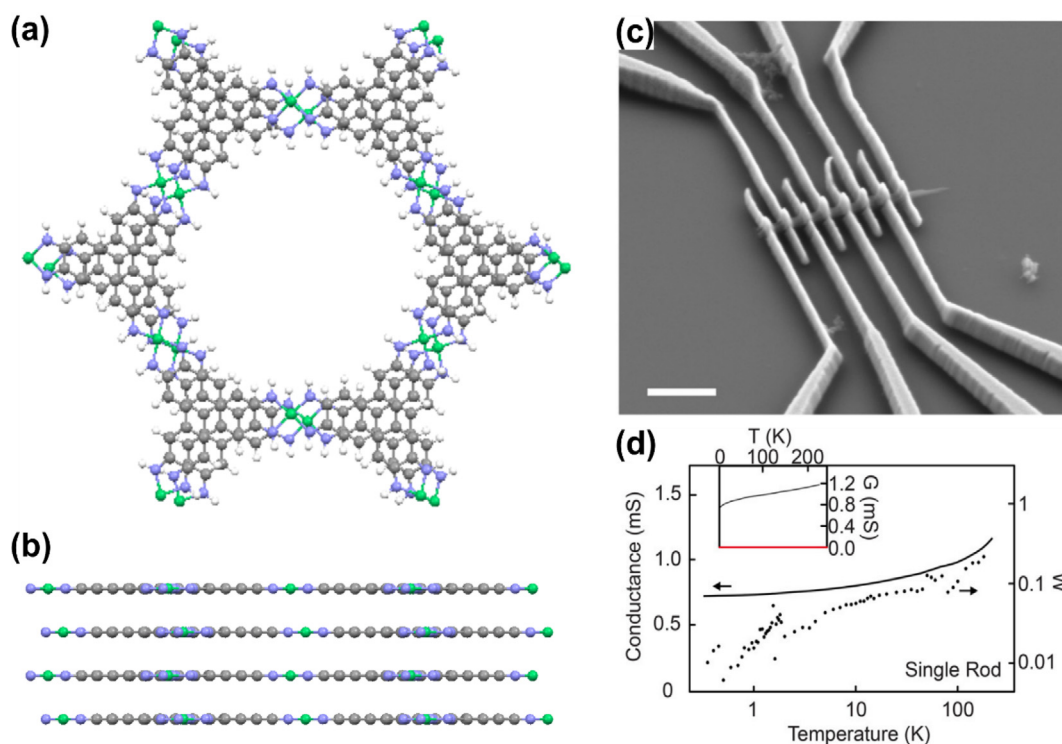
Fig. 11. (a) and (b) Top and side view respectively of the 2D layers in the Ni$_3$(HITP)$_2$ structure. (c) SEM image of rod-like Ni$_3$(HITP)$_2$ single crystal device. (d) Temperature dependence of electrical conductivity of a Ni$_3$(HITP)$_2$ single crystal proving the metallic behavior. Images reproduced with permission from [24].

micrometer-long rod-like crystals obtained using hydrothermal synthesis. In this contribution, the authors report conductivities as high as 150 S·cm^{-1} with Ni$_3$(HITP)$_2$ single crystals with non-null conductivities at 0 K, indicating a metallic behavior (Fig. 11c and d) [24]. DFT calculations by Foster *et al.* already demonstrated in 2018 that such differences may arise from interface defects as grain boundaries or stacking displacements, which do not only break the conjugation of the graphitic layers or the charge delocalization across them but also can open a band gap in the otherwise metallic Ni$_3$(HITP)$_2$ MOF [80]. DFT calculations anticipated a semiconductor behavior for a Ni$_3$(HITP)$_2$ monolayer, whereas the bulk material is metallic. A related DFT study anticipated an increase of the band gap upon increasing the intralayer distance [81]. Importantly, a strong band dispersion is not only obtained in the *in-plane* direction but orthogonally to the 2D layers as well, underlining the strong charge delocalization across the layers. Therefore, the relevance of the synthetic protocol is highlighted as it leads to materials with different conductivities as shown in Table 2.

TP-based MOFs as Cu$_3$(HITP)$_2$ [82] and Co$_3$(HITP)$_2$ [25] structures were also synthesized and characterized. The XRD patterns of both MOFs indicated their isostructural nature. However, slight variations on the interlayer distance with the metallic center were determined, being 3.30, 3.16 and 3.29 Å for Ni$_3$(HITP)$_2$, Cu$_3$(HITP)$_2$ and Co$_3$(HITP)$_2$, respectively [25]. Consequently, different conductivity values of 55.4, 0.75 and 0.024 S·cm^{-1} for the pellets were obtained. Controlled modifications of the conductivity and band gap were also achieved by tuning the metallic ratio in a series of alloys M$_n$M'$_{3-n}$(HITP)$_2$ containing pairs of metallic ions (Ni/Co, Ni/Cu, Cu/Co). Differences on the MOFs behavior depending on the incorporating metal atom have been predicted by DFT calculations. As previously commented, calculations on a Ni$_3$(HITP)$_2$ monolayer structure proved a semiconducting band structure with a band gap of 0.13 eV [83]. The metallic Ni^{2+} center showcases a dsp^2 hybridization with the HITP ligand leading to a perfect square planar geometry in the 2D layer. Upon substitution of Ni^{2+} by Cu^{2+}, a sp^3 hybridization occurs due to the additional electron when comparing the electronic configuration between both ions. Consequently, a square-grid coordination geometry, which induces a distortion in the 2D layers, is obtained. This change in the crystallographic network generates a metallic behavior of the 2D monolayer. However, direct correlation of the different reported crystalline structures with their conductivity values remains a challenge because of the different degree of crystallinity of the pressed pellets, especially in the case of Co$_3$(HITP)$_2$ crystals [25]. Accordingly, it is clear that the variability of the chemical formula

of the TP-based MOF will have a direct impact not only in possible applications of these materials but also in the control that can be exerted in their crystalline structure (see *vide infra*). It was only recently that large conductivities in Co$_3$(HITP)$_2$ crystals have been reported by Zhi and co-workers upon their post-synthetic treatment by liquid exfoliation reaching values of 67.8 S·cm^{-1} [84]. Interestingly, novel chemical formula Mn$_3$(HITP)$_2$ is also reported in this work, proving to be isostructural to Co$_3$(HITP)$_2$ crystals.

3.1.3. THT-based 2D MOFs

The first reported THT-based 2D MOF consisted of crystals with Pt as metallic ion grown through an in situ reaction between a metallic salt and THT in the presence of oxygen [90]. After the MOF formation, the THT ligand was in a −4 oxidation state, which caused the uptake of sodium ions to balance the charge, reaching the final formula of Na$_{1.8}$Pt$_3$(THT)$_2$. The square planar coordination geometry favored the formation of hexagonal layered networks with a staggered stacking due to the large ionic radius of Pt ions (see Fig. 12a and b). Importantly, the THT ligands could be further oxidized upon I$_2$ treatment reaching a neutral formula of Pt$_3$(THT)$_2$ without no relevant structural changes and a final conductivity of the order of 10^{-6} S·cm^{-1}. This low value arises from the lack of *out-of-plane* contribution as staggered packing alternates the TP moieties, disabling their interaction. Further, Pt is a very large metallic ion that cannot form strong d-π bonds leading to a weak intralayer charge delocalization.

To improve the conductivity, other smaller metallic ions were tested, such as Co and Ni, whose bis(dithiolene) complexes have proved a strong bonding with large carrier mobilities and several accessible redox-active states [18,55]. Hence, in 2015, Marinescu and co-workers reported the Co$_3$(THT)$_2$ MOF with honeycomb 2D layers stacked with an eclipsed conformation that resulted in conductivities of 1.4·10^{-3} S·cm^{-1} for pressed pellets and 3.2·10^{-2} S·cm^{-1} for thin films formed through an interfacial reaction method, without any further treatment [55]. DFT calculations suggested that these conductivities were associated with an *out-of-plane* mobility, with low *in-plane* conductivities arising from the mixed-valence character of the metallic centers (two Co^{3+} per Co^{2+} center). Note that the Co$_3$(THT)$_2$ MOF transitions from a semiconducting state, attributed to a scattering of charge carriers at high temperatures, to a metallic state upon decreasing the temperature are strongly dependent on the pellet/film thickness. Dong *et al.* also reported the growth of a 2D monolayer of the complex Ni$_3$(THT)$_2$ using the Langmuir-Blodget technique. The single-layer exhibited a hexagonal pattern with pores of ~2 nm and large

Table 2
Conductivities of HATP-based MOFs.

MOF	Measuring technique	Conditions	Conductivity (S·cm^{-1})	Orientation	Ref
Ni$_3$(HITP)$_2$	Single crystal (4-probe)	Vacuum	150	*c*-axis	[24]
	Film (2-probe)	Ambient	39.7	ab-axis	[63]
	Film (2-probe)	Ambient	7.5·10^{-4}	c-axis	[63]
	Film (vdP)	Vacuum	40	Random	[35]
	Film (-)	–	37.2	Random	[85]
	Film (2-probe)	–	8.5·10^{-3} −0.23	Random	[57]
	Pellet (vdP)	Vacuum	50	Random	[86]
	Pellet (vdP)	Vacuum and annealing	58.8	Random	[87]
	Pellet (4-probe)	Ambient	55.4	Random	[25]
	Pellet (4-probe)	–	39	Random	[76]
	Pellet (4-probe)	Ambient	1.896	Random	[88]
	Pellet (4-probe)	–	1	Random	[89]
	Pellet (2-probe)	Vacuum	2	Random	[35]
Cu$_3$(HITP)$_2$	Pellet (2-probe)	Ambient	0.2	Random	[82]
	Pellet (4-probe)	Ambient	0.75	Random	[25]
Co$_3$(HITP)$_2$	Pellet (4-probe)	–	67.8	Random	[84]
	Pellet (4-probe)	Ambient	8·10^{-4}	Random	[88]
	Pellet (4-probe)	Ambient	0.024	Random	[25]
Mn$_3$(HITP)$_2$	Pellet (4-probe)	–	44.92	Random	[84]
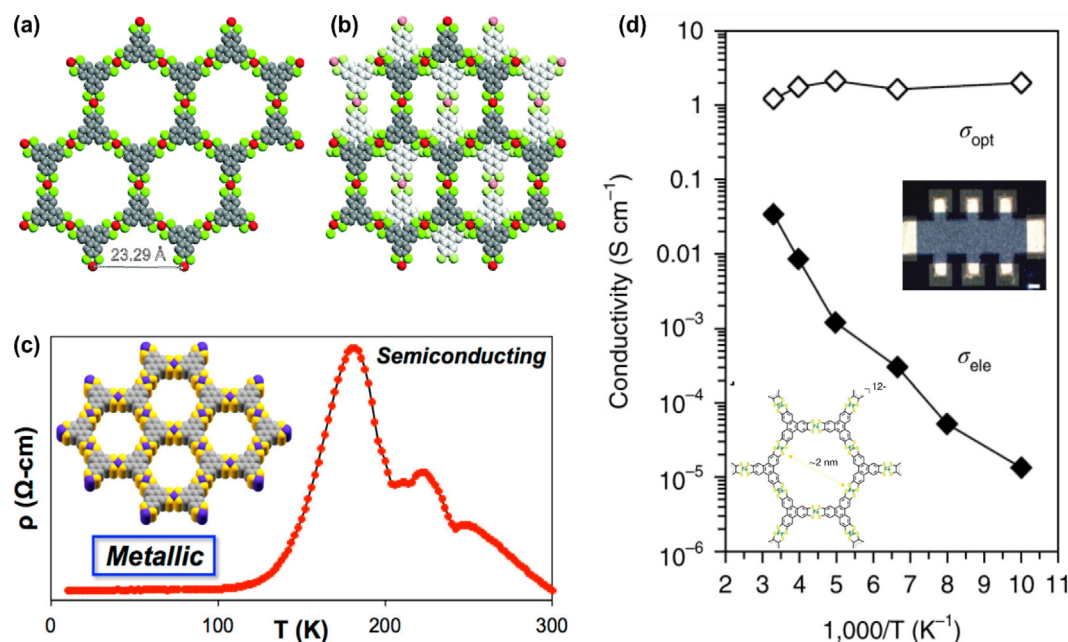
Fig. 12. (a) and (b) Single layer and layer packing structures of $Pt_3(THT)_2$ crystals. Images reproduced with permission from [90]. (c) Temperature dependance of the electrical resistivity of $Co_3(THT)_2$ samples passing from a semiconducting to metallic behavior. The eclipsed honeycomb structure of $Co_3(THT)_2$ is shown in the inset. Image reproduced with permission from [91]. (d) Electrical (full dots) and optoelectrical (empty dots) conductivity of $Fe_3(THT)_2$ thin films. The thin film device and structure of $Fe_3(THT)_2$ are shown in the inset. Images adapted from [92].

stability, with a large lateral area in the order of millimeters, and thicknesses of 0.7 nm.

In 2017, Mirica and co-workers reported the hydrothermal synthesis of $Co_3(THT)_2$, $Cu_3(THT)_2$ and $Ni_3(THT)_2$ MOFs under basic conditions [93]. The spectroscopic characterization evidenced the mixed valence character of cobalt and copper metal centers (Co^{2+}/Co^{3+} and Cu^{1+}/Cu^{2+}), whereas only the Ni^{2+} state was found. Pressed pellets of the resulting polycrystalline material showed very low conductivities of $2.4 \cdot 10^{-9}$, $2.4 \cdot 10^{-8}$ and $3.6 \cdot 10^{-4}$ S·cm^{-1} for $Co_3(THT)_2$, $Cu_3(THT)_2$ and $Ni_3(THT)_2$, respectively. Thin films of the $Fe_3(THT)_2(NH_4)_3$ MOF with good control on their thickness were reported by Feng and co-workers in 2018 using a liquid–liquid interfacial approach [92]. The Fe ions were found in its Fe^{3+} state, despite using Fe^{2+} ions as reactive materials. Hence, in order to compensate the charge of the fully anionic THT ligand, ammonia ions were incorporated in the structure. Crystallographic analysis revealed hexagonal layers packed in a near-eclipsed inclined structure with conductivities of $3.4 \cdot 10^{-2}$ S·cm^{-1} and semiconductor behavior with optical band gaps of 245 meV. Hence, time-resolved photoconductivity measurements were performed, reaching mobilities of up to 220 cm^2 V^{-1} s^{-1}. Marinescu and co-workers demonstrated similar semiconductor to metallic transitions in this material with conductivities of ~ 0.2 S·cm^{-1} for as-synthesized specimens [94]. Importantly, upon oxidation to atmospheric air, the semiconductor-to-metal transition temperature shifted to

higher values, reaching room temperature metallic behavior and final conductivities of $8.0 \cdot 10^{-4}$ S·cm^{-1}. Table 3 summarizes the reported conductivities of THT-based 2D MOFs synthesized under different conditions.

3.1.4. Other structures

The development of new structures were firstly anticipated by DFT calculations for systems combining dual ligands or different hetero-atom substitutions in ortho position of Pt and Pd TP-based MOFs [95,96]. These variations on previously described structures evidenced their great impact on the band structure of the material as different band gap openings were obtained. These indications were further explored experimentally by developing novel hetero-atom substitutions or by combining different ligands.

The quest for novel structures was realized by the combination approach of two or more ligands within a single structure. For example, Feng and co-workers reported the simultaneous incorporation of HATP and THT ligands into a honeycomb structure obtained as a crystalline powder or thin films (either monolayer or supported on graphene) [97]. Control on coordination spheres is hardly achieved obtaining randomly distributed CoN_2S_2, CoN_4 and CoS_4 coordination units along the material (Fig. 13a). The CoN_2S_2 center contributed to an enhanced catalytic activity caused by the combination of donor atoms contributing each to the absorption and desorption of analytes.

Table 3
Conductivities of THT-based MOFs.

MOF	Measuring technique	Conditions	Conductivity (S·cm^{-1})	Orientation	Ref
$Ni_3(THT)_2$	Pellet (-)	–	$3.6 \cdot 10^{-4}$	Random	[93]
$Cu_3(THT)_2$	Pellet (-)	–	$2.4 \cdot 10^{-8}$	Random	[93]
$Co_3(THT)_2$	Film (vdP)	–	$3.2 \cdot 10^{-2}$	Random	[91]
	Pellet (vdP)	–	$1.4 \cdot 10^{-3}$	Random	[91]
	Pellet (-)	–	$2.4 \cdot 10^{-9}$	Random	[93]
$Fe_3(THT)_2$	Film (vdP)	Vacuum	$3.4 \cdot 10^{-2}$	Random	[92]
	Film (vdP)	Vacuum	0.2	Random	[94]
$Pt_3(THT)_2$	Pellet (2-probe)	–	$3.86 \cdot 10^{-4}$	Random	[90]
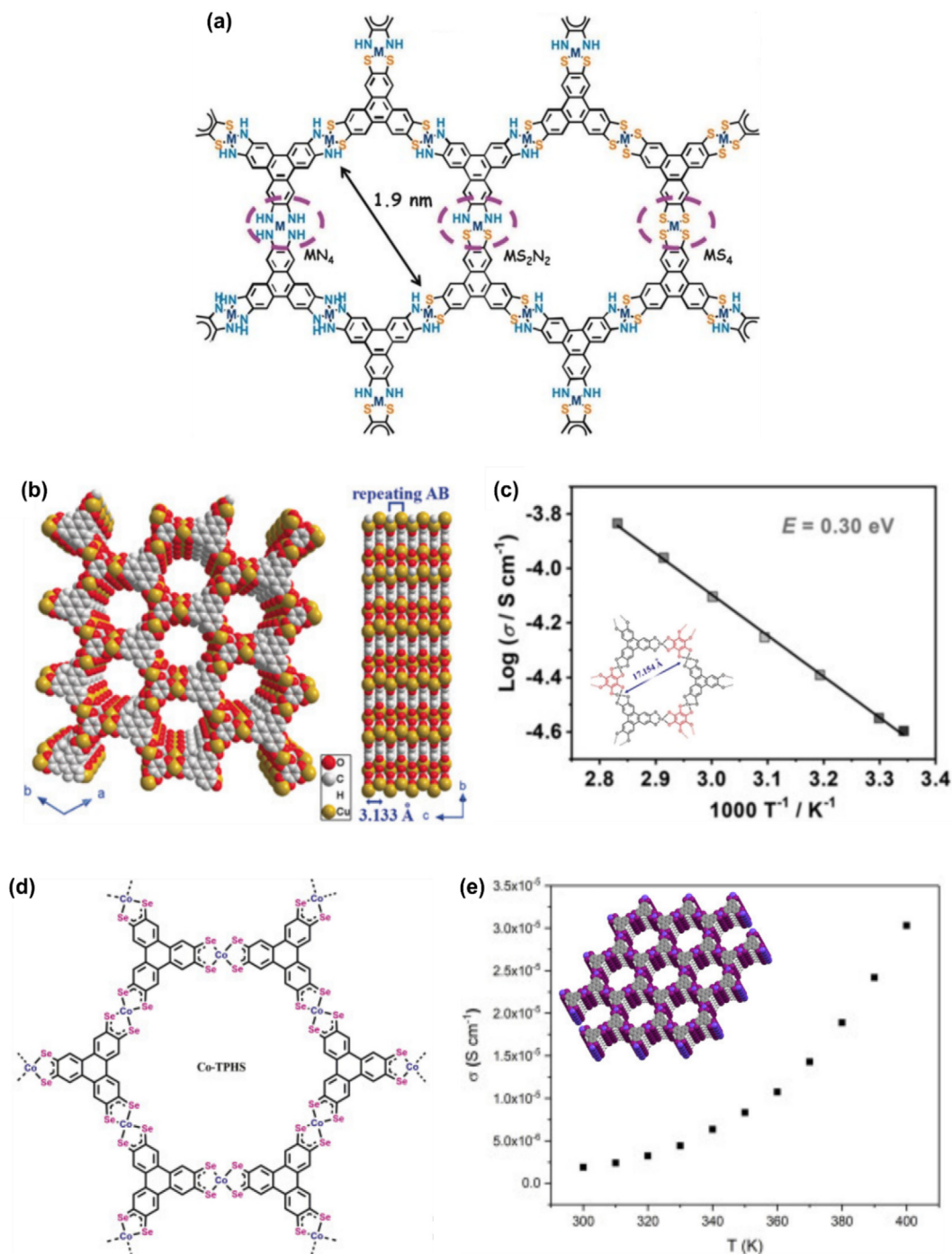
Fig. 13. (a) Structure of the honeycomb lattice incorporating both THT and HATP molecules. The different available coordination spheres (CoN_4, CoN_2S_2, CoS_4) are shown. Image reproduced with permission from [97]. (b) Top view and side view of the $Cu_3(HHTP)(THQ)$ structure. (c) Temperature dependance of the electrical conductivity of $Cu_3(HHTP)(THQ)$. Inset: Structure of a single layer of $Cu_3(HHTP)(THQ)$. Images reproduced with permission from [98]. (d) Structure of a single layer of $Co_3(TPHS)_2$. (e) Temperature dependance of electrical conductivity of $Co_3(TPHS)_2$. Inset: Eclipsed packing structure of the layers in $Co_3(TPHS)_2$. Images reproduced with permission from [99].

Kitagawa and co-workers reported the combination of alternating HHTP and tetrahydroxy-1,4-quinone (THQ) ligand within the semiconducting $Cu_3(HHTP)(THQ)$ MOF [98]. Enthylenediamine, as a chelating agent of the metallic center, was required in the synthesis in order to ensure the coordination balance between the two units, while avoiding the precipitation of $Cu_3(HHTP)_2$ or $Cu_3(THQ)_2$ MOFs. Hexagonal layers pilled in a slipped parallel fashion (pores of 1.7 nm) with conductivities of $2.53 \cdot 10^{-5}$ S·cm^{-1} (Fig. 13b and c) were obtained.

A selenol-based triphenylene (TPHS) ligand was used to synthesize a semiconducting TP-based 2D MOF, i.e. $Co_3(TPHS)_2$, with an eclipsed packing of 2D layered hexagonal honeycomb (Fig. 13d and e) [99]. The conductivity of a pressed pellet was in the order of 10^{-6} S·cm^{-1} because of the poor crystallinity of the material in the stacking direction. DFT calculations on the structure revealed a poor electronic coupling of the d and π orbitals of the Co and ligand respectively, probably caused by the large radius of the Se donor atom. This led to larger interlayer contribution to the

electronic coupling. Strikingly, $Co_3(TPHS)_2$ showed glassy magnetic properties with low intralayer antiferromagnetic coupling.

3.2. Applications of triphenylene-based 2D MOFs

In this section, some of the most characteristic applications explored for these materials are listed with a correlation (if applicable) of the chemical structure on the performance of the material.

3.2.1. Chemiresistive sensor

TP-based 2D MOFs have proved to be largely sensitive to ambience conditions [100]. The conductivity of this MOF family can reach larger values in vacuum while in ambience, inert conditions or when exposed to acidic/basic media, the conductivity values decrease considerably. Thus, this property has naturally opened the way to chemiresistive gas sensing applications of these materials. Many examples of TP-based 2D MOF sensing devices can be found in the literature, as for instance sensing humidity [26] or toxic gases (NH_3, NO or H_2S) [33,36,38,82]. Additionally, devices have been adapted to a wide variety of platforms, including electronic textiles [36], flexible polymers [26,38] or pressed pellets [33]. Note that all devices showcase ppm range sensitivity and detection limits, and fast responses (both detecting and recovery). Choosing an appropriate combination of metal and ligand has proved to be critical as different responses to the analytes are obtained for each MOF (Fig. 14a and b). Most frequently the ligands used in this application are HATP or HHTP incorporating Ni or Cu as metal ions.

In a very recent study, Mirica and co-workers demonstrated that different host guest interactions between MOF and ammonia gas took place depending on the used ligand and metal [101]. In all cases, the MOF electronic structure was altered upon the interaction with ammonia, while preserving the crystallinity of the material. In the case of amino-substituted TP-based MOFs, NH_3 is adsorbed at Lewis acid sites without causing structural changes. However, in the case of hydroxyl-substituted TP-based MOFs, ammonia coordinates to Brönsted acid sites inducing structural changes in the TP aromatic ring, affecting the MOF's conductivity (Fig. 14c). Moreover, Cu-based MOFs seemed to display larger redox reactivity by coordination to ammonia than Ni-based ones. Thus, Cu-based MOFs are, in principle, more suitable materials for chemiresistive sensors of basic gases than Ni-based. In contrast, Ni-based MOFs seem more suitable to detect neutral volatile organic compounds such as ethanol, acetone or aromatic volatile molecules (Fig. 14d) [102]. Consequently, Cu-based MOFs have been more widely used for highly selective sensing of ammonia traces in interference gases as ethanol or acetone [51] contrarily to Ni-based MOFs. Note that apolar volatile molecules are hardly detected by TP-based 2D MOFs chemiresistive devices. Driven by the success in chemiresistive sensor applications, TP-based 2D MOFs are currently studied for the detection of other analytes employing potentiometric [29] (ionic salt concentration) and neurochemical voltammetry sensors [30].

3.2.2. Batteries/Supercapacitors

The large conductivity and surface area of TP-based 2D MOFs led to large capacitance when incorporating them in pressed pellets electrodes. Further, their large 1D pores allow to host large and solvated ionic structures making them suitable for supercapacitors or ion batteries [79,86]. In 2017, Dincă and co-workers reported the first TP-based MOF electrode for supercapacitors using pressed pellets of $Ni_3(HITP)_2$ with capacities of up to 18 $\mu F \cdot cm^{-2}$, exceeding values found for some other carbon-based materials [86]. Moreover, the electrodes proved large stability, retaining almost 90% of the capacitance after 5000 charge and

discharge cycles. Interestingly, the MOF-based supercapacitor was used as battery for flashlight. Similar capacitive values were obtained with $Cu_3(HHTP)_2$ electrodes used in zinc batteries, retaining also 75% of the initial capacity after 500 cycles [79]. Notoriously, $Cu_3(HHTP)_2$ electrodes possessed two redox-active sites (the copper ion and the quinoid structure) to increase the specific capacity of the material in a reversible way, storing the Zn^{2+} ions in the 1D pores. Nevertheless, pelletization of the TP-based 2D MOFs dramatically decreases the available surface area, hindering the internalization of ions into the structure [37,41].

Nanostructuration of a TP-based MOF electrode has been recently reported as an approach to increase the available surface area. In a first example, $Cu_3(HHTP)_2$ nanowires were grown on carbon paper by the template-assisted method leading to large surface areas of 540 $m^2 \cdot g^{-1}$ without the need for further treatment (Fig. 15a) [37]. Remarkably, the supported carbon paper electrodes displayed capacities of 22 $\mu F \cdot cm^{-2}$, which were retained up to 80% of the initial value after 5000 cycles. Furthermore, larger capacitive responses of 3200 $mF \cdot cm^{-2}$ were obtained in hybrid nanostructured porous arrays obtained by combining $Ni_3(HHTP)_2$ nanorods grown on top of double layered NiCo hydroxide nanosheets in a Ni foam [41]. Another example of a hybrid material used for the fabrication of a supercapacitor was the growth of $Ni_9(HHTP)_4$ on 3D porous laser-scribed graphene (LSG) interdigitated electrodes on polyimide substrates (Fig. 16a–c) [103]. LSG was patterned applying a CO_2 laser and a O_2-plasma prior to growth of the MOF on the surface. The hybrid MOF/LSG material provided large areal capacitance, energy density and power density (15.2 $mF \cdot cm^{-2}$, 4. 1 $\mu W \cdot h \cdot cm^{-2}$ and 7 $mW \cdot cm^{-2}$ respectively). Another strategy to increase charge percolation and available surface area consists of growing TP-based 2D MOFs on top of flexible structured substrates as polypropylene separators [85] (Fig. 15b–d) or cellulose nanofiber papers (Fig. 16d–g) [76]. The obtained composites exhibited large conductivities along with large areal capacities, which were preserved after several charge–discharge cycles.

3.2.3. Electrocatalyst

The large conductivity and porosity of TP-based 2D MOFs together with their large metallic active site density have encouraged their use as electrocatalysts. Note that they have been reported to effectively perform electrochemical redox reactions in fuel cell batteries for hydrogen evolution reaction (HER) or oxygen reduction reaction (ORR). CoS_4 metal–organic centers previously proved to have large catalytic activity for HER. In 2015, Marinescu *et al.* reported the use of $Co_3(THT)_2$ thin films as an electrocatalytic cathode for hydrogen generation from water [55]. The film was synthetized by the interfacial method and deposited onto a variety of substrates (HOPG, glassy carbon...). The electrode proved to be suitable for HER reactions as it exhibited both high stability against acids and large cobalt active site density. Tafel slopes of 189 $mV \cdot dec^{-1}$ at pHs of 4.2 were reported.

On the other hand, ORR reactions are apparently less efficiently catalyzed depending on the used structure. In a primary study, $Ni_3(HITP)_2$ film grown on glassy carbon electrodes displayed large ORR activity under O_2 atmosphere [104]. Interestingly, the electrodes remained essentially stable with values of 88% of the initial current in the potentiostatic measurement retained over 8 h. However, the reaction was strongly dependent on the pH of the media, suggesting that the electron transfer mechanism was modified along with the pH. Theoretical insights on the catalytic mechanism for the oxygen reduction reaction on $M_3(HITP)_2$ (M = Ni, Cu) proved that generation of H_2O_2 under acidic conditions is more favorable in both structures due to the complicated multipath generation of H_2O [105]. Consequently, an insightful investigation was followed, where the effectivity of different TP-based 2D MOFs for ORR was studied [77]. In this research, Dincă and co-workers
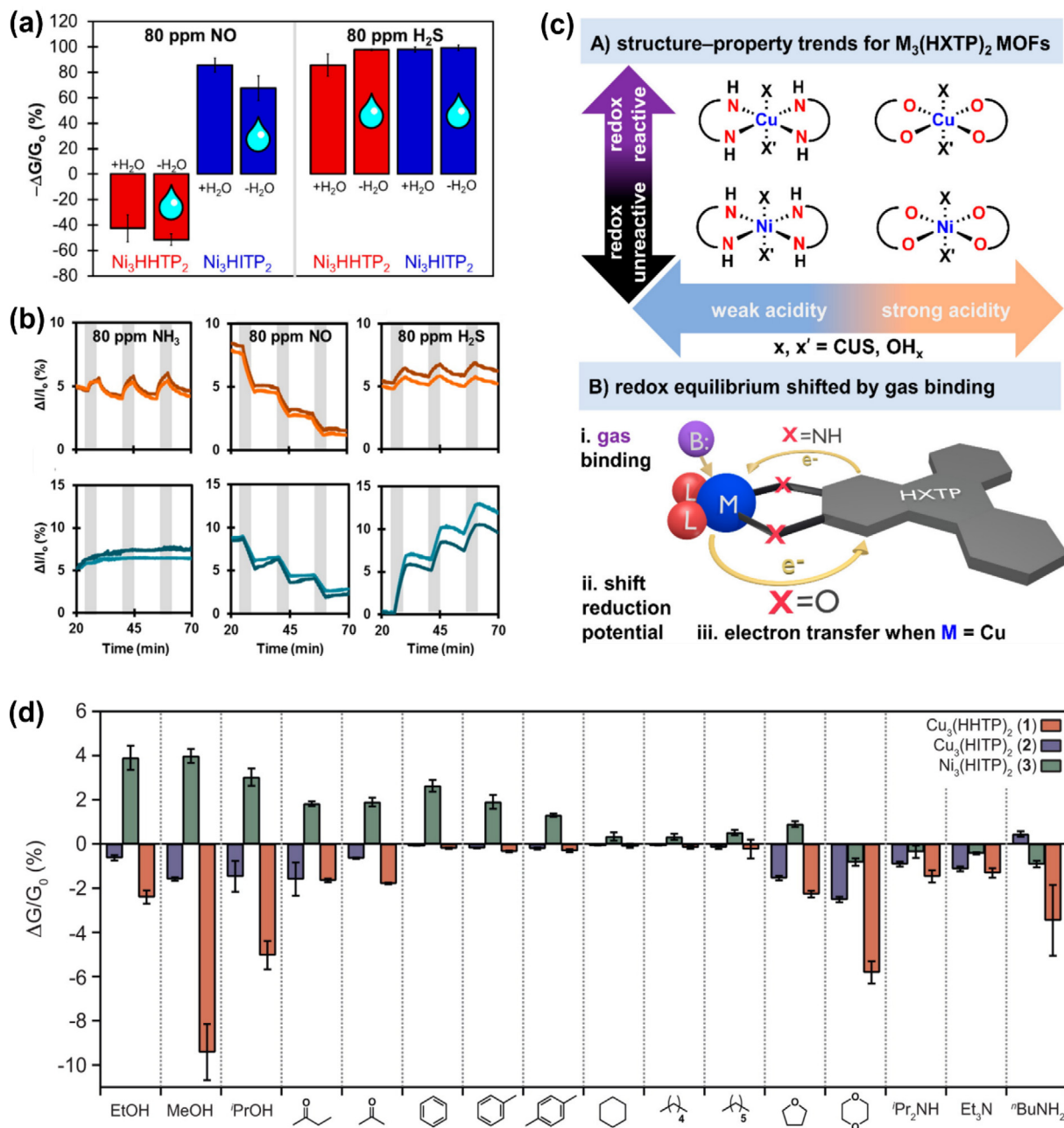
Fig. 14. (a) Saturation sensor response for electronic textiles containing $Ni_3(HHTP)_2$ (red) and $Ni_3(HITP)_2$ (blue) exposed to 80 ppm of NO and H_2S in dry nitrogen (solid bars) and in the presence of 5000 ppm water (with water droplet). Relevance of the used ligand in the MOF is shown, as different responses are obtained between the two systems having the same metallic ion. Image reproduced with permission from [36]. (b) Sensing traces of toxic gases NH_3, NO and H_2S at 80 ppm using $Cu_3(HHTP)_2$ (orange) and $Ni_3(HHTP)_2$ (blue) grown on flexible devices. Grey areas represent the exposure of the devices to the respective gas. Relevance of the used metal in the MOF is highlighted in this figure as different responses are obtained for a same analyte. Image reproduced with permission from [38]. (c) Summary of the general trends in acidity and redox activity of MOFs probed by basic gases and proposed mechanism for the shift of oxidation states in Cu-containing species upon binding of a basic gas. Image reproduced with permission from [101]. (d) Sensor responses of chemiresistors arrays of $Cu_3(HHTP)_2$, $Cu_3(HITP)_2$ and $Ni_3(HITP)_2$ to different analytes. Image reproduced with permission from [102].

reported the higher catalytic activity of hexagonal crystalline systems such as $Ni_3(HITP)_2$, $Cu_3(HITP)_2$ and $Cu_3(HHTP)_2$. The high electrical conductivity and redox activity of these systems facilitated the electron transfer to O_2. In contrast, trigonal crystallized MOFs as $Ni_3(HHTP)_2$ and $Co_3(HHTP)_2$ have a distortion of the π-π stacking of the triphenylene cores, which strongly affects the electron transfer kinetics. Hence, the crystalline structure is critical to determine the electrocatalytic properties of TP-based 2D MOFs. Interestingly, large electronic density of $M_3(HITP)_2$ structures has also proved to be suitable for other electrochemical reactions such

as O_2 generation [106] (enhanced by doping of the structure with iron catalytic centers) and CO_2 reduction, mimicking photosynthesis processes [107,108]. Large photocatalytic performance was obtained under light irradiation when using $Ni_3(HITP)_2$ as co-catalyzer along with a photosensitizer [108].

3.2.4. Spintronics

Cu-based MOFs have been the widest explored materials for these properties due to their electronic configuration with an odd number of d electrons. In a recent study published by Dincă *et al.*,
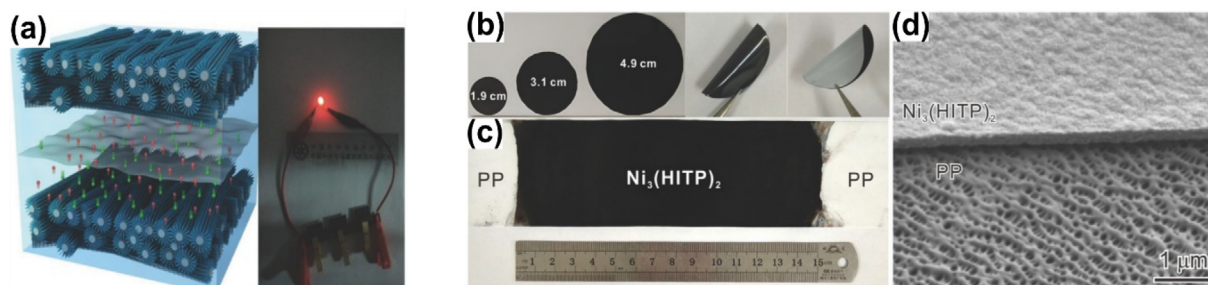
Fig. 15. (a) Schematical structure of $Cu_3(HHTP)_2$ on carbon paper supercapacitor (left) and photograph of a red light-emitting-diode powered by the three supercapacitors connected in series (right). Image reproduced with permission from [37]. (b) and (c) Photographs of the $Ni_3(HITP)_2$ grown on polypropylene separators showing their different shape and sizes and their flexibility. (d) SEM cross-section image of $Ni_3(HITP)_2$ films on polypropylene. Images reproduced with permission from [85].
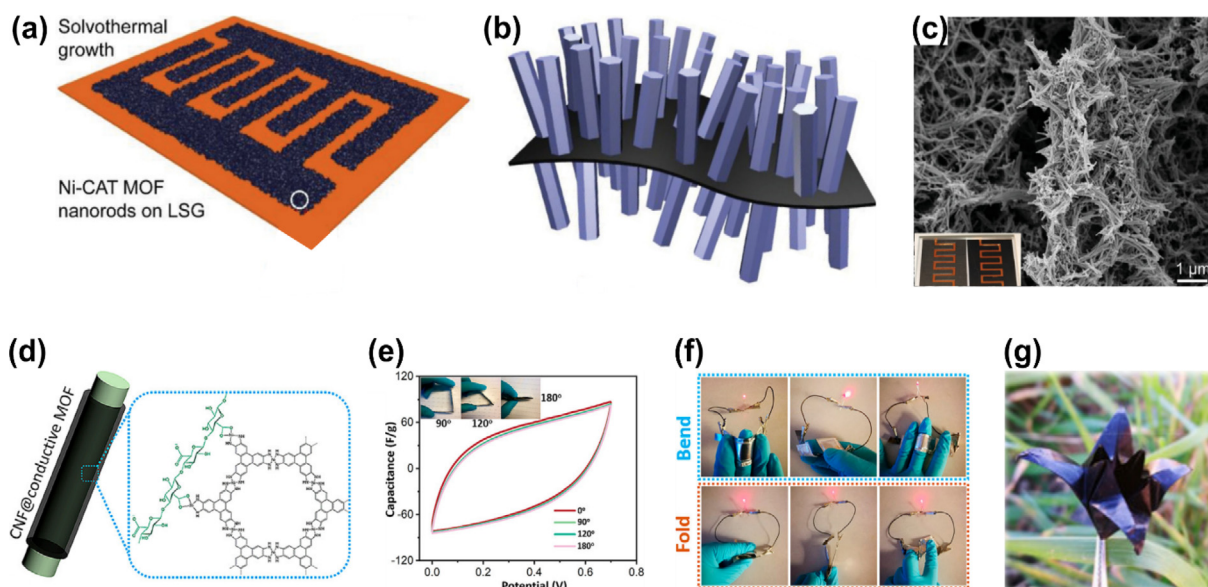
Fig. 16. (a) Schematic and structural illustrations of the interdigital pattern of $LSG/Ni_9(HHTP)_4$ hybrid and (b) solvothermal growth of $Ni_9(HHTP)_4$ nanorods. (c) SEM image of the structure of $LSG/Ni_9(HHTP)_4$ hybrid showing the large available porosity. Images reproduced with permission from [103]. (d) Schematic illustration of the growth of $Ni_3(HITP)_2$ and $Ni_9(HHTP)_4$ on cellulose nanofiber papers. (e) Cyclic voltammetry measurements of $Ni_3(HITP)_2$ on cellulose paper at different folding angles. (f) Photographs of red light-emitting diodes powered by $Ni_3(HITP)_2$ on cellulose paper capacitors under different folding or bending geometries. (g) Photograph of origami folded $Ni_3(HITP)_2$ on cellulose paper capacitors in flower shape. Images reproduced with permission from [76].

single crystals of trinuclear molecular models of $Cu_3(HHTP)_2$ and $Cu_3(HITP)_2$ MOFs were obtained, being analogous coordination systems to TP-based MOFs [109]. Magnetic measurements on these crystals displayed antiferromagnetic coupling of neighboring spins, which could effectively lead to spin frustration if occurring in the TP-based 2D MOFs. This effect has been deeper studied recently by Awaga and co-workers, who demonstrated that thin films of $Cu_3(HHTP)_2$ exhibit antiferromagnetic interactions between neighboring atoms, and that TP-based 2D MOF can reach a quantum spin liquid state at ultralow temperature (38 mK) [78]. This property has paved the way to novel spintronic applications for their use as organic spin valves [49]. Highly oriented thin films of $Cu_3(HHTP)_2$ were implemented on vertical spin valves devices between LMSO and Co ferromagnetic electrodes. The chemical structure and rational *c*-axis growth of the film enabled the spin-polarized transport through the MOF. The devices showcased low magnetoresistances at cryostat temperatures that were retained upon changing the film thickness and increasing the temperature up to 200 K.

On the other hand, possible presence of spin in Ni-complexes was assessed very recently by the study of a trinickel molecular model of $Ni_3(HHTP)_2$ subjected to different redox reactions [110].

Interestingly, changes on the oxidation state do not occur on the metallic center but at the TP core giving rise to closed shell, monoradical and diradical species. Consequently, the increase of the oxidation state led to a decrease on the spin coupling strength.

3.2.5. Optoelectronics

Thanks to their large conjugation, this family of MOFs exhibit a strong light absorption with chemically tunable band gaps. The large variability on chemical structures in TP-based 2D MOFs also enables the tuning on the optoelectronic properties as shown by Zhang *et al.* recently [111]. In their work, different $M_3(HITP)_2$ structures showcased different non-linear optical absorbance due to the increasing number of d electrons. These effects gave relevance in optoelectronic devices such as photodetectors or solar cells. In 2019, Bein and co-workers reported on basic photovoltaic devices by implemented highly oriented $Ni_3(HHTP)_2$ thin films grown on ITO through vapor-assisted conversion [52]. Interestingly, photoinduced charge generation and separation could be observed in the MOF film, making this material suitable for solar cell devices. The devices showcased open-circuit voltages of 156 mV under irradiation. Furthermore, Feng and co-workers reported recently a $Fe_3(THT)_2$ photodetector capable of detecting radiation ranging
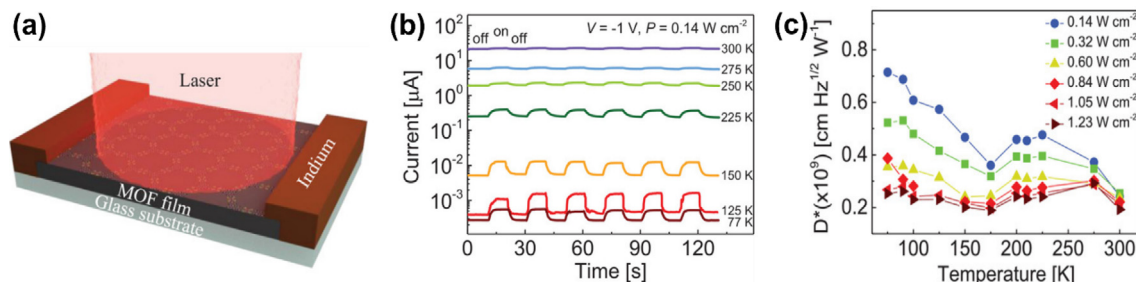
Fig. 17. (a) Schematic illustration of a Fe₃(THT)₂ thin film photodetector device with indium electrodes. (b) Temperature-dependent photoswitching behavior under pulsed illumination of 785 nm laser. (c) Temperature dependence of photodetection at different power densities. Images reproduced with permission from [112].
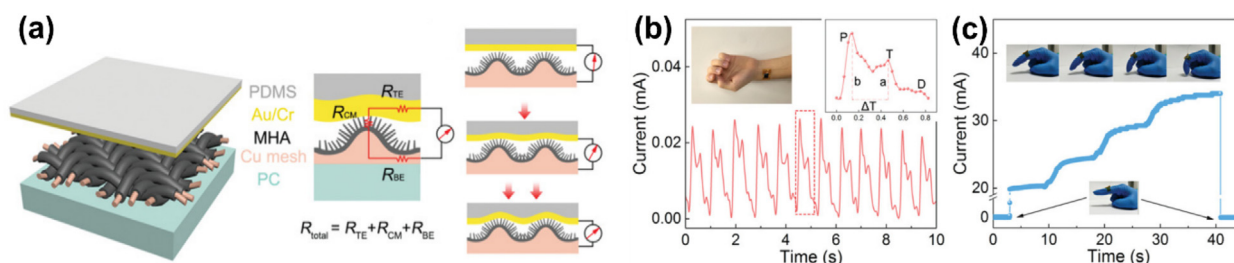
Fig. 18. (a) Schematic illustration of the working principle of a MOF-based tactile sensor. Larger applied pressure leads to larger contact area between the MOF-containing mesh and the top electrode film and therefore the lower measured resistance. (b) Heart-beat monitoring using the MOF-based tactile sensor. (c) Current monitoring at different finger bending angles. Images reproduced with permission from [40].

from UV to the NIR (400–1575 nm) (Fig. 17a) [112]. Owing to the narrow IR band gap of the material, room-temperature detection was limited. A good performance was reported at cryogenic temperatures with specificities of $7 \cdot 10^8$ cm·Hz$^{1/2}$·W^{-1} (Fig. 17b and c).

3.2.6. Tactile sensor

The template-assisted growth of the Cu₃(HHTP)₂ on Cu(OH)₂ microwires grown on a flexible Cu mesh substrate was used to develop a tactile sensor [40]. The rationally designed flexible sensor allowed for the modulation of the contact area as a function of the applied pressure, having a direct impact on the measured intensity (Fig. 18). This was used to monitor human motion and pulse, recognizing music through machine learning algorithms and displaying pressure maps when using an array of multiple sensors. Remarkably, the sensor showcased a large durability, retaining nearly all the initial signal after 2700 pressure and release cycles.

3.2.7. FET logic

In 2014, Xu *et al.* reported porous FET transistors based on thin films of Ni₃(HITP)₂ [58]. The highly smooth and compact thin films were obtained by interfacial liquid–air method and recovered by stamping on a silicon wafer for its integration into a FET transistor. The transistor revealed a p-type behavior with large hole mobilities of up to 48.6 cm²·V^{-1}·s^{-1}. Other electronic features of the device as large on/off ratios pointed to future possible applications as voltage-gated ion channels.

3.2.8. Thermoelectric

The combination of low thermal conductivity derived from the strong phonon scattering of the porous of this family of MOFs together with their high electrical conductivity has open new avenues for their use in thermoelectric applications. Nanostructuration and grain boundaries also avoid phonon propagation, decreasing thus the thermal conductivity. However, only the thermoelectric properties of Ni₃(HITP)₂ pressed pellets have been

reported with an ultralow thermal conductivity of 0.21 W·m^{-1}·K^{-1} and a large electrical conductivity of 58.8 S·cm^{-1} [87]. Remarkably, Ni₃(HITP)₂ pellets provided negative Seebeck coefficients, indicating an n-type thermoelectric behavior, and high thermoelectric figure of merit (ZT) of $1.19 \cdot 10^{-3}$ at room temperature. In complementary studies, crystallinity of the material was crucial as it deeply impacts the electrical conductivity and subsequently, the thermoelectric efficiency [89].

4. Triphenylene-based 2D COFs

4.1. Chemical families

In this section, we describe different families of TP-based COFs grouped according to the used ligand.

4.1.1. HHTP-based 2D COFs (ester-boronate and polyarylether bonds)

The most common family of HHTP-based COFs, and arguably of all TP-based COFs, is that formed from boronic acids that covalently react upon dehydrogenation generating five-membered BO₂C₂ rings. A prototype structure of one of such ester-boronate COFs is the COF-5 reported by Yaghi and co-workers by condensing the hydroxyl derivative triphenylene HHTP and 1,4-benzenediboronic acid (BDBA) in a three-day solvothermal synthesis (Fig. 19) [23,34]. Crystallographic characterization revealed a hexagonal unit cell forming layers stacked in an eclipsed boron nitride arrangement with interlayer distances of 0.34 nm as in graphitic structures. This structure leads to a large porosity showcasing 1D mesopores of 27 Å in diameter. Interestingly, the eclipsed layer stacking is attributed to the presence of triphenylene cores, as they interact by π-π stacking. Afterwards, the synthesis protocol has been extended to a wide variety of boronic acid derivatives giving rise to numerous TP ester-boronate COFs, named after COF-5 as COF-6, COF-8 and COF-10 [113], most of them summarized in Fig. 19. Most of them retain the crystalline space group of COF-5 with planar layers and porous diameters ranging from the
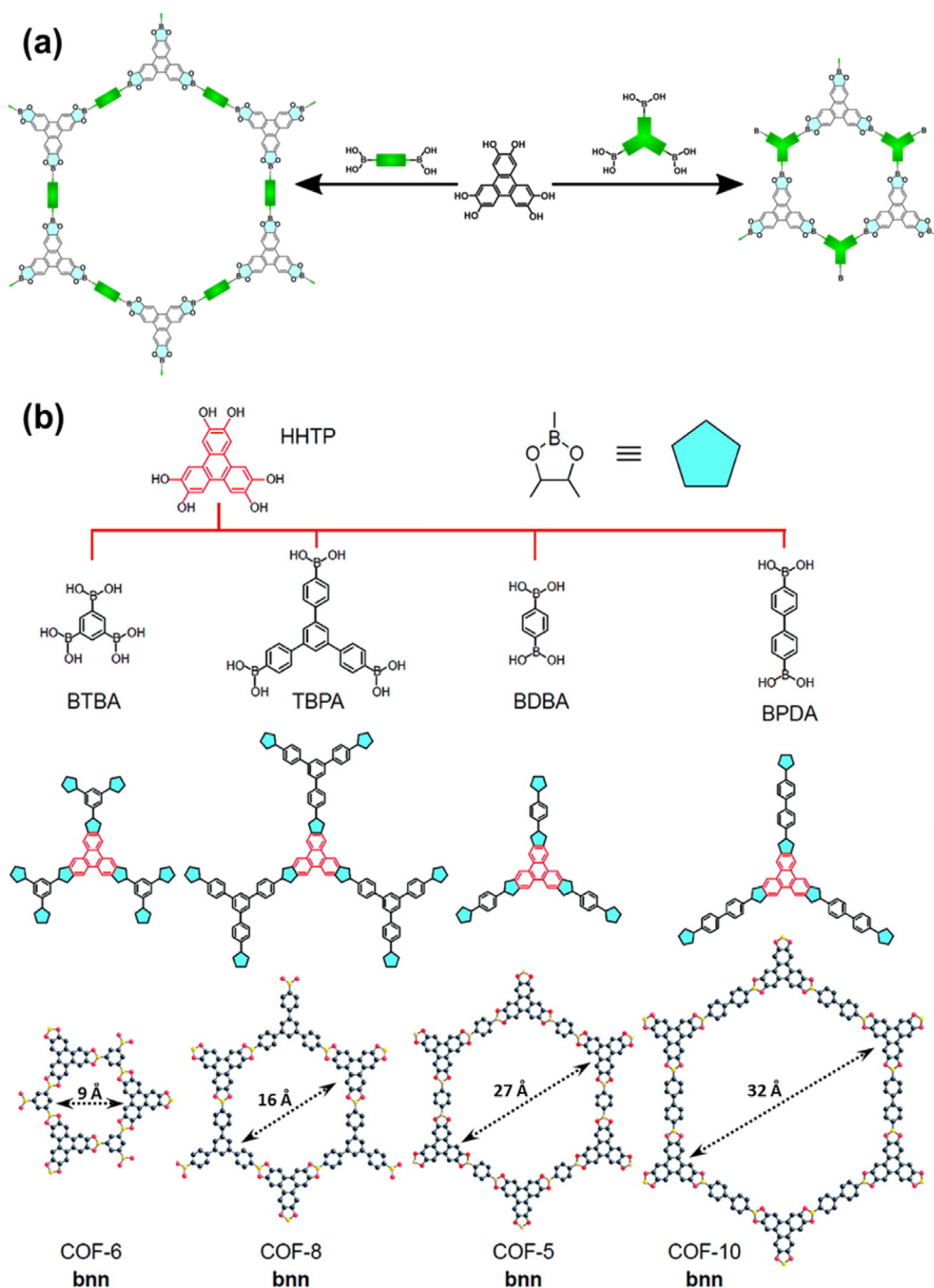
Fig. 19. (a) Schematic of the structures of ester-boronate TP-based COFs condensing di- or tri-boronic acids with HHTP. (b) Condensation reactions between boronic acids and HHTP giving rise different TP-based 2D COFs with different porosities. B, orange; O, red; C, black. All COFs have a boron-nitride (bnn) layer packaging. Image adapted from [114].

angstrom to the few nanometers, and therefore variable adsorption surface areas [114].

Ester-boronate TP bonding can be combined with other condensation reactions in the same synthesis, which enables a rational design of novel COFs. Jiang and co-workers reported numerous TP-based COF structures combining boron-ester and imine condensation reactions [115] in tri-ligand fused synthesis as the one presented in Fig. 20a. Different functionalities were achieved by modifying the employed boronic acid. Simultaneously, Zeng *et al.* reported the synthetic study of the same structure [116]. Despite these efforts, crystallization could only be achieved in one-pot reaction in the presence of all three ligands, as sequential

condensations would lead to either other boronic structures or the lack of precipitate. However, the obtained TP-based COF exhibited a large H_2 and CO_2 uptake with BET surface areas of 1619 $m^2 \cdot g^{-1}$. Polyarylether TP-based 2D COF structures have been recently developed by nucleophilic aromatic substitution between *ortho*-difluoro benzene derivatives and HHTP [117]. Two layered structures, JUC-505 and JUC-506 (Fig. 20b) were obtained using tetrafluoroterephtalonitrile and 2,3,6,7-tetrafluoroanthraquinone, respectively. Both structures exhibit hexagonal pores of 16.8 and 28.4 Å, respectively, and large chemical stability in strong acid, basic, reductive or oxidant media. Incorporation of cyano groups in JUC-505 as shown in Fig. 20b allowed for post-synthetic
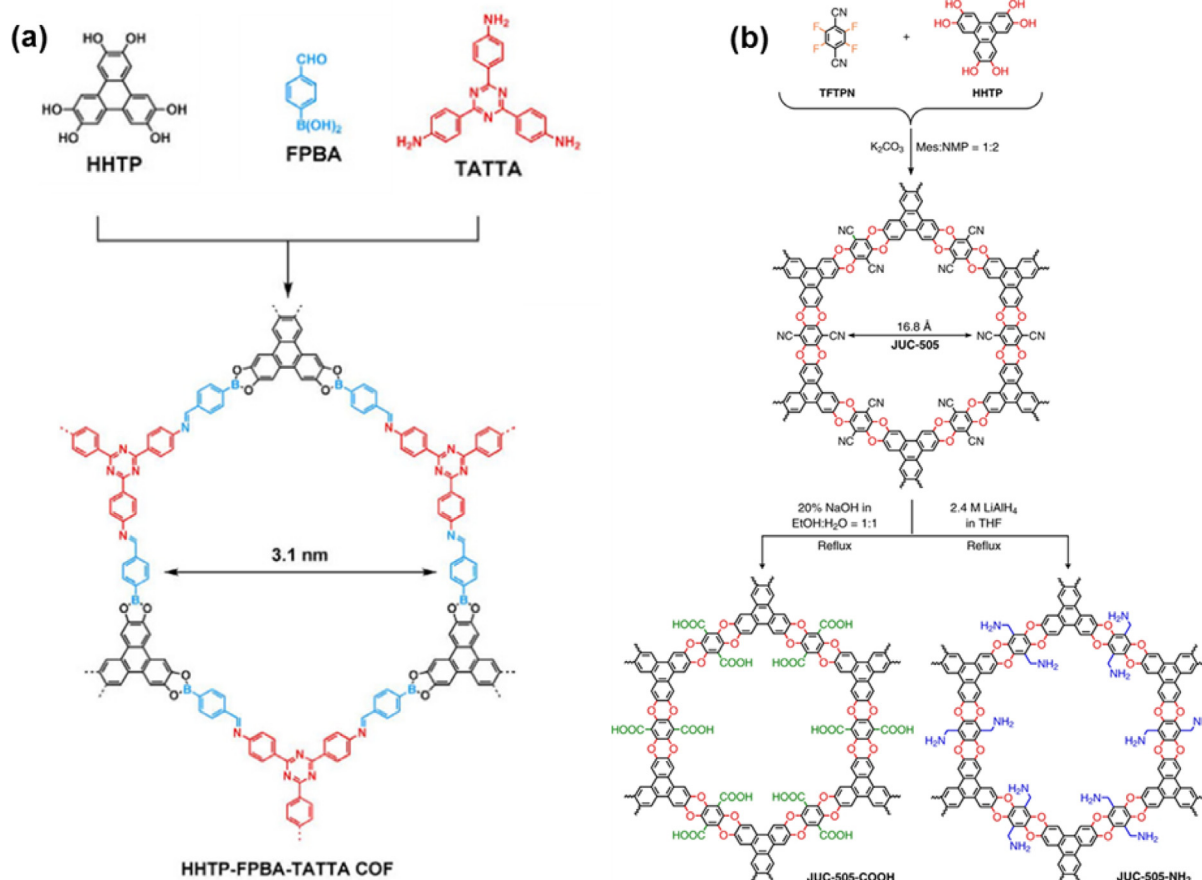
Fig. 20. (a) Synthesis of a multi-valent hexagonal TP-based COF using boron-ester and imine condensation reactions. Image reproduced from [115]. (b) Synthesis of JUC-505 through the condensation of tetrafluobenzenes and HHTP. The CN groups in the structure enable the generation of JUC-505-COOH and JUC-505-NH$_2$ structures via post-synthetic reactions. Image adapted from [117].

functionalization with carboxyl or amino groups forming JUC-505-COOH and JUC-505-NH$_2$ structures, respectively. The same strategy was performed by Yaghi and co-workers to synthesize amide and amidoxime groups in the COF structure [118].

A wide variety of TP-based 2D COFs with ester and ether bonds using HHTP can be synthesized depending on the targeted application. Novel structures or structural modifications have been investigated mainly aimed at gas storage applications (H$_2$, CH$_4$, CO$_2$...), especially with boronic ester COFs, as the boronic acid determines the porous size and surface area, and therefore, the gas uptake capability [23,114]. Analogously, pore size modifications and chemistry surface functionalization on polyarylether structures allows for tailoring the uptake of chemical species into the pores, enabling water treatment and filtration applications at various pHs [117,119]. Note that electronic applications of these structures are hardly explored since ester and ether bonds break the conjugation along the 2D layer. A clear example of this is their recent use in low-k dielectrics [47]. Thus, charge transfer occurs mainly in the *out-of-plane* direction through the one-dimensional stacking of TP moieties, similarly as it occurs for DLCs. Hence, doping is often required for optoelectronic applications, either by incorporation of electron donor/acceptor atoms into the ester/ether structure [120], use of conjugated ligands (creating electron donor–acceptor systems along with TP) [121] or external optoelectronic doping [44]. All these aspects are summarized in Table 4, which comprises investigated TP-based boronic ester-linked COFs and their properties and applications to date. Note that optoelectronic features are not commonly found in the literature for these materials. An in-depth description of the properties and applications of the structures described with different acids can be found in Section 4.2.
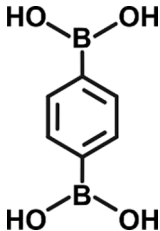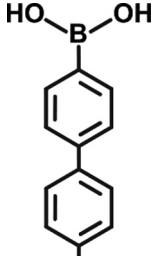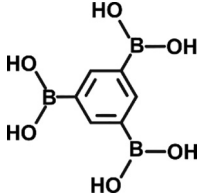
4.1.2. HATP-based 2D COFs (phenazine bonds)

Inspired by the successful synthesis and application of ester and ether COFs, other TP-based 2D COFs have been recently reported employing other condensation reactions. Phenazine-fused TP-based COFs is a main example of novel structures obtained by the imine condensation reaction. Phenazine-fused TP-based 2D COFs comprise nitrogen-doped graphitic porous structures with *in-plane* charge transfer features. These tailored structures are suitable for electronic applications owing to their large electronic conjugation (see Section 4.2 for more information). Typically, they are formed in solvothermal conditions by condensation of HATP with *ortho*-planar tetraketones [32,149,150]. As previously indicated for ester/ether COFs, different ketones can be used as starting monomers to tailor the porous size as shown in Fig. 21. Fig. 21b shows the CS-COF structure obtained by Guo *et al.* in a reaction between HATP and *tert*-butylpyrene tetraone, which led to an extended π-conjugated system with pores of 1.6 nm [32]. Fig. 21a depicts a structure reported by Meng *et al.* as a result of condensing HATP and hexaketonecyclohaxane into a layered 2D COF with 1D pores of diameter ~1 nm [149]. Note-worthy, in this work, the TP-based 2D COF proved to have low conductivities of the order of 10^{-8}–10^{-9} S·cm^{-1} under anhydrous conditions at 323 K whereas under 97% relative humidity, the conductivity increased to $1.51 \cdot 10^{-5}$ S·cm^{-1}, indicating a large proton conductivity. The conductivity values were further increased by acidification

Table 4
Described boronic COFs.
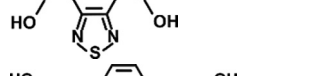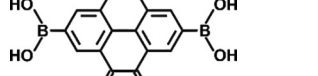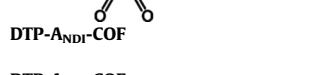
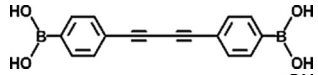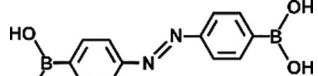| COF /Boronic acid used	Form	Synthesis method	Pore size (Å)	BET Surface area (m²·g⁻¹)	Properties and application	Ref
(1,4-benzenediboronic acid structure)	Powder	Solvothermal	27	1590	H_2 uptake	[23,122]
	Powder	Solvothermal	–	1990	H_2, CH_4, CO_2 uptake	[114]
	Powder	Solvothermal	–	2000	Synthesis studies	[28]
	Powder	Solvothermal	–	1517	–	[123]
	Powder	Solvothermal	2.274–1.248	1421–36	Tunable porosity	[124]
	Powder	Solvothermal	27	1670	Mechanistic studies of synthesis	[125]
	Powder	Solvothermal	–	–	Growth kinetic study in homogenous reaction	[126]
	Powder and oriented pressed pellets	Solvothermal and high pressure pelletization	–	–	Li-Ion battery	[127]
	Powder	Microwaved assisted synthesis	–	2019–2027	Synthesis studies	[128]
	Powder	Microwaved assisted synthesis	–	1200	Synthesis studies	[129]
	Powder	Sonochemistry	–	–	Starting material for B-doped molten salt synthesis	[130]
	Powder	Sonochemistry	–	–	Stability in different pyridine percentages	[131]
	Powder and supported thin film	Sonochemistry with substrate imbedded in solution	–	2122	Synthesis studies	[27]
	Powder and free-standing thin film	Solvothermal and solvent evaporation for thin film	–	840 (Thin film)	Synthesis studies (for colloidal suspension)	[132]
	Supported thin film	Vapor-assisted conversion	27	–	Preferential orientation, control of thickness and different substrates	[53]
	COF coating of CNTs and graphene	Sonochemistry with substrate imbedded in solution	–	57.6/9.83	CO_2 uptake	[45]
	COF coating on polydopamine coated glass	Solvothermal	–	–	Electrochromatography of small molecules	[46]
	COF coating on CNTs	Solvothermal with substrate imbedded in solution	–	–	Li-Ion battery	[44]
(4,4'-biphenyldiboronic acid structure)	Supported monolayer	UHV evaporation	29.8	–	–	[69]
	Powder	Solvothermal	34.1	2080	Gas uptake	[113]
	Powder	Solvothermal	32	1320	Mechanistic studies of synthesis	[125]
	Powder	Solvothermal	34	1200	Ammonia uptake	[133]
	Powder	Sonochemistry	–	–	Stability in different pyridine percentages	[131]
	Powder	Solvothermal	–	2080	H_2, CH_4, CO_2 uptake	[114]
	Powder	Solvothermal	–	–	Synthesis studies	[126]
	Powder	Solvothermal	–	–	Synthesis studies (for colloidal suspension)	[132]
	Supported monolayer	Solvothermal with substrate imbedded in solution	–	–	–	[68]
(benzene-1,3,5-triboronic acid structure)	Powder	Solvothermal	6.4	980	Gas uptake	[113]
	Powder	Solvothermal	–	960	H_2, CH_4, CO_2 uptake	[114]

Table 4 (*continued*)

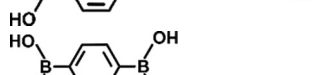| COF /Boronic acid used	Form	Synthesis method	Pore size (Å)	BET Surface area (m²·g⁻¹)	Properties and application	Ref
(structure: triphenylbenzene triboronic acid)	Powder	Solvothermal	18.7	1400	Porosity	[113]
	Powder	Solvothermal	–	1400	H$_2$, CH$_4$, CO$_2$ uptake	[114]
	Nanosheets	Liquid phase exfoliation of powder assisted by sonication	17	–	Nanostructuration	[134]
(structure: pyrene diboronic acid)	Powder	Solvothermal	32	868	Gas uptake, Fluorescence and Conductivity	[135]
	Powder	Solvothermal	–	–	Synthesis studies	[126]
	Powder	Solvothermal	–	–	Synthesis studies for colloidal suspension	[132]
	Supported thin film	Solvothermal with substrate imbedded	32	–	Photoemission	[43]
(structure: benzodithiophene diboronic acid)	Powder	Solvothermal	25.7	904	Compared to other tiophene based COFs and doping with oxidizing agents	[120]
	Powder	Solvothermal	29 with ethoxys	1844 with ethoxys	Synthesis studies and tunable porosity	[136]
	Powder	Solvothermal	–	1125 (S) 1056 (Se) 302–352 (Te)	Tunable conductivity (substitution of sulfur with other chalcogenides)	[137]
	Powder and thin film	Solvothermal and spin-coating for film	30	1810	Photovoltaics: Adsorption of fullerenes as host–guest for photoluminescent quenching	[138]
	Powder and oriented thin films	Vapor-assisted conversion	32	1946 (powder) 175–145 cm²/cm² (thin films)	Photovoltaics: Adsorption of fullerenes as host–guest for photoluminescent quenching	[48]
	Powder and supported thin film	Solvothermal with substrate imbedded	–	1376 (powder)	Both randomly and oriented films. Photoconductivity: Faster response in oriented.	[31]
	Oriented thin films	Vapor-assisted conversion	32	–	Conductivity anisotropy measurements and hole photoconductivity	[139]
	Thin film	Vapor-assisted conversion	32	990	Control of preferential orientation and thickness on different substrates	[53]
	Powder	Solvothermal	–	2400	Synthesis studies	[126]

Table 4 (continued)

COF /Boronic acid used	Form	Synthesis method	Pore size (Å)	BET Surface area (m²·g⁻¹)	Properties and application	Ref
	Powder	Solvothermal	–	–	Synthesis studies (for colloidal suspension)	[132]
	Powder and supported thin film	Solvothermal with substrate imbedded	47	2640	Gas uptake, control on preferentially oriented films and blue emission	[140]
	Powder	Solvothermal	30	810	Isomerization with UV radiation with retention of porosity and structure	[141]
	Supported monolayer	UHV evaporation	36	–	–	[142]
	Powder and supported thin film	Solvothermal with substrate imbedded	28	2021	Photoconductivity	[121]
	Powder	Solvothermal	32	1510	Large interlayer interaction with antiparallel building blocks	[143]
DTP-A$_{NDI}$-COF	Powder and coating of CNTs	Solvothermal with presence CNTs	50.6	1583 (powder) 676 (CNT)	Li-ion battery	[144]
DTP-A$_{NDI}$-COF DTP-A$_{PyrDI}$-COF	Powder	Solvothermal	53 53	1504 1910	Photoluminiscence kinectic studies	[145]
TDB (**1**) TDB (**2**) BTDB (**3**)	Powder	Solvothermal	20.6 (**1**) 13.8 (**2**) 32.4 (**3**)	972 562 544	Synthesis studies and conductivity by doping with oxidizing agents	[120]
T-COF-OH	Powder	Solvothermal	41	2000 560 (post-functionalization)	Post-synthesis chemical modifications	[146]
Porphyrin	Powder and supported thin film	Solvothermal with substrate imbedded	46	8.9	Photovoltaics	[147]
Combination of different acids	Powder	Solvothermal	–	–	Multifunctional COFs	[148]

of the COF by impregnating it with 12 M H_3PO_4 up to a value of $1.23 \cdot 10^{-3}$ $S \cdot cm^{-1}$ under hydration conditions of 97% at 323 K.

Interestingly, this structure could also be obtained by inverting the functional groups of the starting materials, in other words, by condensing HHTP molecules with planar tetraamines [151]. Strikingly, nitrogen-doped TP-based 2D COFs with larger pores can be obtained upon the reaction between HHTP and HATP as reported by Jhulki *et al.* [152] with the structure of C2P-5 COF. Analogous structures were reported by Liu and co-workers, by Buchwald-Hartwig cross-coupling reaction between hexabromotriphenylene and HATP [153]. Interestingly, both eclipsed and staggered packing were obtained. All the structures hereby described present an eclipsed packing of the layers, thus *out-of-plane* contribution is expected as well, either by delocalization of the electrons in the TP moieties or by proton conduction along the one-dimensional porous.

4.1.3. Other structures

Research on different polymerized triphenylene structures has enabled the realization of new carbon allotropes such as TP-based graphdyine (TP-GDY) analogues, containing both *sp* and *sp²* carbon atoms. This structure is well characterized, including its large electronic conjugation, which makes TP-GDY suitable for electronic applications. Nishihara and co-workers reported the synthesis of TP-GDY by means of Glaser-Hay homo-cross coupling catalyzed by copper in a liquid–liquid interfacial system obtaining thin films of 220 nm thickness [154]. Later, Tan and co-workers reported modifications of the synthesis, which allowed the manufacturing of nanosheets and thin films with thicknesses of few monolayers (0.9 nm) and good mechanical strength [59].

4.2. Applications of TP-based 2D COFs

A particular property of layered COFs is their large π-orbital overlap in the stacking direction conferring them both high exciton and charge conduction, which are interesting features for optoelectronic applications. Furthermore, their large and extended porosity enable chemical encapsulation or electrochemical doping for complementary functionalities. Finally, their high thermal stability prevents phase transitions that impair or inactivate their electronic properties. However, to aim to given properties or applications, one might tailor the structure of the COF or shape it in a given fashion.

4.2.1. Photovoltaics and photocurrent

Free TP molecules exhibit a characteristic blue emission fluorescence that is usually shifted upon integration in a COF structure as a result of a higher delocalization degree when conjugated co-ligands are present [135,140,155]. These structures are characterized by the overlap of the TP emission band with the co-ligand absorption one, acting as a donor–acceptor system (where the TP is an electron donor and the co-ligand an electron-acceptor). Interlayer distance is a critical feature in some cases, and enables on/off phosphorescence at cryogenic temperatures upon its reduction [155]. Interestingly, several studies have reported that photoluminescent kinetics is highly dependent on crystallites size, with shorter exciton life times for suspensions containing smaller particles [156,157].

Control over the charge transfer in donor–acceptor systems suggests potential photovoltaics applications. Several ester-boronate COFs have been described including TP and the boronic acid as electron donor and an acceptor moiety, respectively [121,145,147]. The eclipsed stacking of the layers in these structures led to bicontinous electron donor–acceptor ordering: upon light irradiation hole charge transfer is driven through the one dimensional stacking of TP moieties, whereas electron conduction

is ensured by the eclipsed packing of the acceptor units. For example, Jiang and co-workers reported a boronic ester COF with a benzothiadiazole boronic acid serving as electron acceptor [121]. This structure provided large photocurrents with hole and electron mobilities of 0.01 and 0.04 cm^2 V^{-1} s^{-1}, respectively. The same strategy was used by Bein and co-workers in a donor–acceptor system comprising a porphyrin TP-based COF (Fig. 22b and c). A highly oriented thin COF film was incorporated in a photovoltaic device, which reached open-circuit voltages of 312 meV [147]. External doping agents such as fullerene derivatives can be used as acceptors when hosted in the one-dimensional pores of the electron donor COF (Fig. 22a) [138]. Nonetheless, such heterojunctions can limit the charge separation and mobility, and hence, the photovoltaics performance.

Large *in-plane* conjugation of TP-based COFs may also enable the generation of photocurrents. A clear example is the previously introduced phenazine-fused CS-COF structure seen in Fig. 22d and e. The extended π-conjugated system exhibited a large hole photocurrent mobility (4.2 cm^2 $V^{-1} \cdot s^{-1}$) [32]. However, faster photoconductive kinetics were obtained by hosting C_{60} fullerenes molecules in the pores of CS-COF as a donor–acceptor system as it occurred for previously described structures. Further, the CS-COF ⊃ C_{60} system was successfully integrated into functional photoswitches and photovoltaic cells. Similarly, previously introduced C2P-5 thin films showcased an intrinsic large hole mobility resulting into conductivities of 1.75 $S \cdot cm^{-1}$ [152]. This conductivity is significantly increased upon irradiation with light especially after hybridization of the C2P-5 films with graphene. Larger photocurrents were recorded when applying larger powder light sources. Thus, the hybrid device proved to be a suitable photodetector for UV, visible and NIR light.

4.2.2. Li-ion battery

As a result of the large conjugation and porosity, the phenazine-fuse COF (Fig. 21a) has a large proton conduction, which can be enhanced in aqueous and acidic media. This property makes this material suitable as an electrode in a battery cell [149]. Performance of this material as anode in Li-ion batteries was studied by Shi and co-workers, which reported high reversible capacities of 701 $mA \cdot h \cdot g^{-1}$ and long cycling performance (up to 4500 cycles) [158]. Similarly, piperazine-based structures with larger pores provided large capacities of 1644.3 $mA \cdot h \cdot g^{-1}$ [153]. Other conjugated graphitic structures, such as TP-GDY, can be considered as suitable candidates for working anodes in Li-ion batteries. For example, hybridization of TP-GDY with CNTs through π-π stacking was performed obtaining free-standing films has been reported [59]. The films exhibited good electrochemical properties with a reversible capacity of 1624 $mA \cdot h \cdot g^{-1}$, good rate performance and recyclability. Furthermore, the hybrid system was incorporated as an anode in a lithium battery. Ester-boronate COFs are rarely used in electronic applications as the boron ester bond breaks the conjugation along the 2D layer. However, one may reach these properties by external doping [44,45,159]. In a recent study, differently charged 2D COFs (COF-5 among them) were doped with low-molecular weight polyethylene glycol (PEG) by including it into their 1D channels [159]. Interestingly, PEG significantly enhanced the Li⁺ ion conduction along the pores of COF thanks to the large amount of oxygen atoms in the PEG structure providing multiple electron donor sites.

4.2.3. Electrocatalysis

Another interesting use of nitrogen-doped COFs is in electrocatalysis. Zhang and co-workers evaluated phenazine-fused COF (Fig. 21a) as an ORR catalyst [160]. DFT calculations revealed that the large nitrogen density, crystallinity and stability of the material supports high availability of electrocatalytic sites. Consequently,
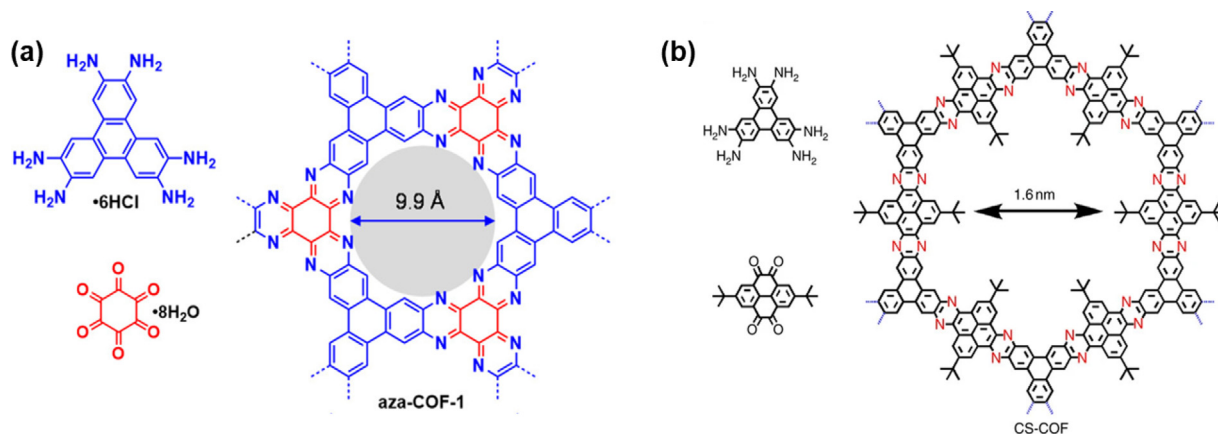
Fig. 21. (a) and (b) Examples of nitrogen-doped graphitic COFs obtained through condensation of HATP with *ortho*-planar ketones. Images adapted from [149] and [32] respectively.

low overpotentials of 349 mV at 10 mA·cm^{-2} and Tafel slopes of 64 mV·dec^{-1} were obtained. The same nitrogen-doped COF have been used to coat composite core–shell structures of Fe/Fe$_3$C nanoparticles in order to improve its long-term stability and performance [150]. Interestingly, the composite exhibited a good electrocatalytic behavior with a 92% retention of the initial current after 10,000 chronoamperometric cycles.

5. Future perspectives

The bourgeoning research in TP-based organic frameworks that followed last few years has led to several discoveries in different fields of applications, where these materials are finding their niche. Undoubtedly, TP-based organic frameworks are significantly skyrocketing in the area of molecular conductors, a field that remains vastly unexplored. TP structures are potential candidates not only because of their electronic properties but also because of their inherent porosity. While benzene ligands enable conductivities within the same range or even larger than TP ligands, in comparison to the latter, benzene ligands have small or inexistent porosity, which significantly hinders the use of these structures in devices such as chemiresistors. Albeit the potential of TP-based MOFs and COFs, the number of reported structures is limited. Rational design has enabled large π-conjugation along the 2D layers and interlayer π-π interactions enabling charge transport pathways, but chemical ligand design is still in its infancy. Novel structures derived from TP substitutions (such as, selenol) or ligand combinations have been recently reported but novel extended ligands containing TP or TP derivative moieties are also arising for both MOF and COF structures [161–164], indicating an exciting yet challenging greenfield.

Most of the conductivities reported for these materials refer to polycrystalline systems, which are not optimal in terms of conductivity. Polycrystalline samples are formed by several finite crystalline domains exhibiting grain boundaries, which disrupt carrier paths and charge transfer, ultimately affecting their conductive properties and, even result in unexpected undesirable properties such as opening a band gap in otherwise metallic materials. Single crystal is a continuous and defect-free (aside from monomer vacancies) structure formed by the infinite repetition of a unit cell. Hence, the properties (including the conductivity) of a single crystal are closer to those intrinsic properties of the material. Hence, single crystals are commonly aimed for the study of anisotropic properties, such as *in-plane* and *out-of-plane* conductivities. Some examples have been reported in the last years especially in the case of TP-based 2D MOFs. Measurements of rod-like

or plate-like single crystals have allowed to assess the correlation of the anisotropy of conductivity with the crystalline structure. However, insights on this correlation are needed as only anisotropy of two structures have been reported in single crystals to date.

The measurement of conductivities of single layers of TP-based systems is timely as atomic- or nearly atomic-thick films will reveal key quantum confinement effects and interlayer interactions. The consequences of shrinking the material to single-layer thicknesses have already been observed in other 2D materials, such as transition metal dichalcogenides. For example, the band gap of MoS$_2$ can be tuned from 1.23 eV in the bulk form to 1.8 eV in the monolayer [165]. Single layers can be obtained using top-down methods, mainly by exfoliating a single crystal, an approach that has already been successfully used for the delamination of 2D coordination polymers [166–168]. However, this requires the growth of crystals sufficiently large, which is a challenging job. While exfoliation of TP-based 2D COFs has been demonstrated in few recent investigations [134], this is not the case for TP-based 2D MOFs. Alternatively, bottom-up techniques represent a strategy that attracts an increasing interest. Among this family of methods, two main methods are particularly appealing such as interfacial liquid synthesis [56] and UHV evaporation, the latter being more suitable to obtain monolayers as the deposition rate allows for an exquisite control over the growth. Reports on the UHV formation of TP-based 2D MOFs and COFs have demonstrated the relevance of several key parameters, such as the deposition order or the stoichiometry between the evaporated monomers [68,142,169]. However, despite numerous studies, only specimens with nanodomains have been accomplished, leading to a finite polymeric array that may be subjected to *in-plane* quantum confinement [68]. Thus, the measured properties may differ from those obtained in an infinite layer. In future, long-range single layers should be obtained and investigated in depth.

Advantages of single crystals prevail for fundamental studies while in terms of applications polycrystalline materials are selected due to the geometrical restrictions to adapt a crystal to a specific device. Thus, development of methodologies that allow for the controlled deposition of the polycrystalline material on substrates to achieve homogenous flat interfaces that avoid charge entrapment have been pursued. Pressing powders into pellets, which can provide smoother surfaces and easily manageable systems is one of the most used methods. However, application of high pressures can induce crystalline phase transitions, crystal breaking, or cause the occlusion of pores. An alternative to postsynthetic treatment consists of directly growing polycrystalline material on supported thin films. This approach can lead to thin films with preferential crystalline orientations that minimize grain
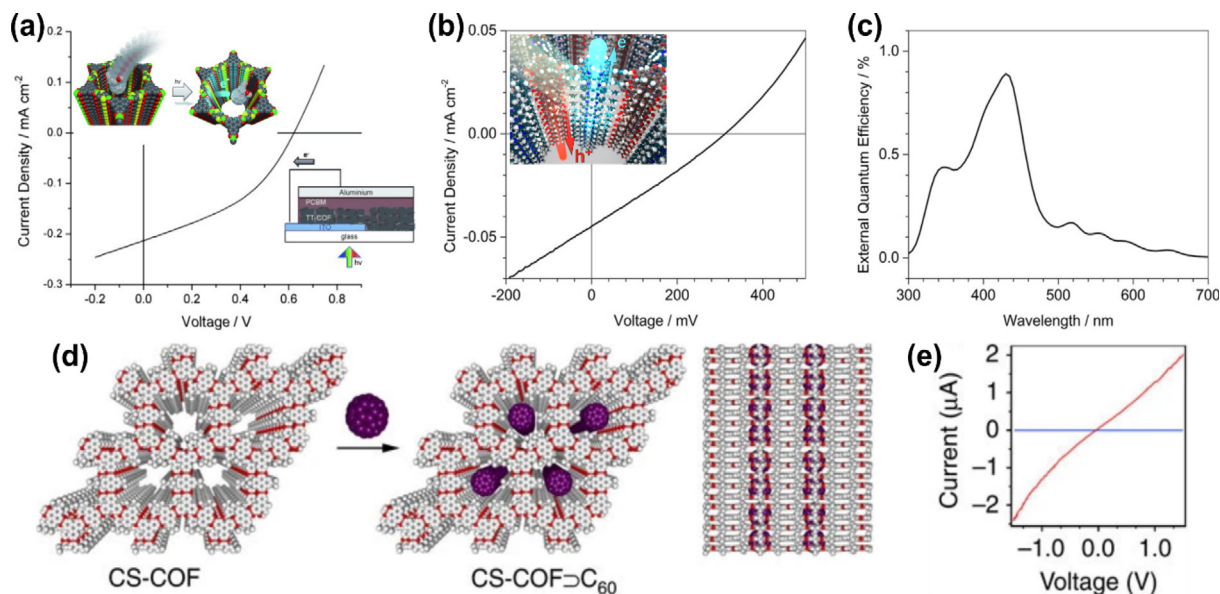
Fig. 22. (a) I–V characteristics of a fullerene-doped thiophene TP-based COF (TT-COF) photovoltaic cell measured under illumination with simulated solar light. Insets: Schematic of the host–guest interaction between the TT-COF and the fullerene derivative (left) and schematic of the photovoltaic device (right). Images adapted from [138]. (b) I-V characteristics under irradiation of a porphyrin TP-based COF acting as a donor–acceptor system. Inset: Schematic of electron and hole charge transfer along the one-dimensional conduction paths defined by the TP and porphyrin moieties. (c) External quantum efficiency of the porphyrin TP-based COF. Images adapted from [147]. (d) Schematic representation of CS-COF and its doping with fullerenes upon host–guest interactions in the open one-dimensional porous channels of the CS-COF (white: carbon; red: nitrogen; purple: fullerene). (e) I-V measurements of the fullerene-doped CS-COF in the dark (blue) and under irradiation (red). Images reproduced with permission from [32].

boundaries and energetic defects while defining the parallel arrangement of one-dimensional pores, charge conduction channels and orbitals. Films obtained by this approach display enhanced performance for applications in photovoltaics [31,48] or spin-valves [49]. Unfortunately, most of current synthetic methods lead to films with sub-millimeter lateral sizes or random crystal orientation. Few examples of oriented thin films of TP-based MOFs and COFs have been reported (mostly limited to HHTP), using layer-by-layer [51] or interfacial approaches [54] (as Langmuir-Blodget or vapor-assisted conversion). Therefore, development of novel synthetic methods that can produce highly oriented thin film morphologies is urgently required. This would include the need to incorporate different compatible substrates aimed at each specific target application. For example, optically transparent or insulating substrates are typically needed for optoelectronic devices, whereas flexible or wearable electronics are more suitable for biological applications. Hence, synthesis protocols need to be compatible with a wide variety of substrates. Finally, methods that can enable the manufacturing of flexible free-standing thin films that can be easily manipulated even in the absence of a support substrate is the need of the hour, which has been only achieved in one occasion to our knowledge [92].

In addition to all of the above, there are two other relevant areas that deserve further studies. The first one is to improve the stability in water. 2D materials are being increasingly used in the biomedical applications, as improved alternatives to established biomaterials. However, the poor stability of TP-based MOFs in water, which causes the material to swell, and possible redox activity of both ligand and metal has significantly prevented their use in this area. TP-based COF structures may have more impact in biomedicine as these materials are more stable in water, while exhibiting proton conductivity in aqueous conditions. Yet, the conductive properties have not been as advanced as they have been for MOFs. Bioelectronic applications of TP-based COFs remain at an earlier stage of development, being the need of doping and lack of intrinsic charge carrier conduction the main limitations in

COF-based systems. Accordingly, further studies are required to improve the stability of TP-based MOFs in water as well as the conductivity of TP-based COFs. Note that in-depth investigations of the magnetic properties of TP-based organic frameworks also remain widely unexplored. In this vein, TP-based 2D MOFs are formed by Kagomé lattice structures, where metallic ions are coordinated in trinuclear arrangements [49,78,109]. Hence, TP-based 2D MOFs are appealing candidates for the generation of geometrically frustrated spin systems. To date, only few examples of Cu-based MOFs have been investigated, and successfully implemented in spin valves. However, both detailed studies to understand and approaches to control the magnetic properties of these materials (with the proper choice of ligands and metals) and their interaction with the conductive properties have been reported. Therefore, we can anticipate a wealth of research in this area over the years to come.

Declaration of Competing Interest

The authors declare that they have no known competing financial interests or personal relationships that could have appeared to influence the work reported in this paper.

References

[1] D. Sonet, B. Bibal, Triphenylene: a versatile molecular receptor, Tetrahedron Lett. 60 (12) (2019) 872–884, https://doi.org/10.1016/j.tetlet.2019.02.033.

[2] S. Ibáñez, E. Peris, A rigid trigonal-prismatic hexagold metallocage that behaves as a coronene trap, Angew. Chem. Int. Ed. 58 (20) (2019) 6693–6697, https://doi.org/10.1002/anie.201902568.

[3] G. Cong, W. Wang, N.-C. Lai, Z. Liang, Y.-C. Lu, A high-rate and long-life organic–oxygen battery, Nat. Mater. 18 (4) (2019) 390–396, https://doi.org/10.1038/s41563-019-0286-7.

[4] S. Kumar, Discotic liquid crystal-nanoparticle hybrid systems, NPG Asia Mater. 6 (2014) e82–e82. https://doi.org/10.1038/am.2013.75.

[5] F.J.M. Hoeben, P. Jonkheijm, E.W. Meijer, A.P.H.J. Schenning, About supramolecular assemblies of π-conjugated systems, Chem. Rev. 105 (4) (2005) 1491–1546, https://doi.org/10.1021/cr030070z.

[6] S. Laschat, A. Baro, N. Steinke, F. Giesselmann, C. Hägele, G. Scalia, R. Judele, E. Kapatsina, S. Sauer, A. Schreivogel, M. Tosoni, Discotic liquid crystals: from tailor-made synthesis to plastic electronics, Angew. Chem. Int. Ed. 46 (26) (2007) 4832–4887, https://doi.org/10.1002/anie.200604203.

[7] T. Wöhrle, I. Wurzbach, J. Kirres, A. Kostidou, N. Kapernaum, J. Litterscheidt, J.C. Haenle, P. Staffeld, A. Baro, F. Giesselmann, S. Laschat, Discotic liquid crystals, Chem. Rev. 116 (3) (2016) 1139–1241, https://doi.org/10.1021/acs.chemrev.5b00190.

[8] K. Nakashima, T. Shimizu, Y. Kamakura, A. Hinokimoto, Y. Kitagawa, H. Yoshikawa, D. Tanaka, A new design strategy for redox-active molecular assemblies with crystalline porous structures for lithium-ion batteries, Chem. Sci. 11 (1) (2020) 37–43, https://doi.org/10.1039/C9SC04175C.

[9] Y.-F. Zhu, X.-L. Guan, Z. Shen, X.-H. Fan, Q.-F. Zhou, Competition and promotion between two different liquid-crystalline building blocks: mesogen-jacketed liquid-crystalline polymers and triphenylene discotic liquid crystals, Macromolecules 45 (8) (2012) 3346–3355, https://doi.org/10.1021/ma300538h.

[10] H.N. Gayathri, B. Kumar, K.A. Suresh, H.K. Bisoyi, S. Kumar, Charge transport in a liquid crystalline triphenylene polymer monolayer at air–solid interface, Phys. Chem. Chem. Phys. 18 (17) (2016) 12101–12107, https://doi.org/10.1039/C5CP07531A.

[11] M. Saleh, M. Baumgarten, A. Mavrinskiy, T. Schäfer, K. Müllen, Triphenylene-based polymers for blue polymeric light emitting diodes, Macromolecules 43 (1) (2010) 137–143, https://doi.org/10.1021/ma901912t.

[12] W. Zheng, C.S. Tsang, L.Y.S. Lee, K.Y. Wong, Two-dimensional metal-organic framework and covalent-organic framework: synthesis and their energy-related applications, Mater. Today Chem. 12 (2019) 34–60, https://doi.org/10.1016/j.mtchem.2018.12.002.

[13] H.-C. Zhou, J.R. Long, O.M. Yaghi, Introduction to metal-organic frameworks, Chem. Rev. 112 (2) (2012) 673–674, https://doi.org/10.1021/cr300014x.

[14] M.S. Lohse, T. Bein, Covalent organic frameworks: structures, synthesis, and applications, Adv. Funct. Mater. 28 (33) (2018) 1705553, https://doi.org/10.1002/adfm.201705553.

[15] J.L. Segura, M.J. Mancheño, F. Zamora, Covalent organic frameworks based on Schiff-base chemistry: Synthesis, properties and potential applications, Chem. Soc. Rev. 45 (20) (2016) 5635–5671, https://doi.org/10.1039/C5CS00878F.

[16] G. Givaja, P. Amo-Ochoa, C.J. Gómez-García, F.F. Zamora, C.J. Gomez-Garcia, F.F. Zamora, Electrical conductive coordination polymers, Chem. Soc. Rev. 41 (2012) 115–147, https://doi.org/10.1039/c1cs15092h.

[17] R. Mas-Ballesté, C. Gómez-Navarro, J. Gómez-Herrero, F. Zamora, 2D materials: to graphene and beyond, Nanoscale 3 (1) (2011) 20–30, https://doi.org/10.1039/C0NR00323A.

[18] L.S. Xie, G. Skorupskii, M. Dincă, Electrically conductive metal-organic frameworks, Chem. Rev. 120 (16) (2020) 8536–8580, https://doi.org/10.1021/acs.chemrev.9b00766.

[19] M. Wang, R. Dong, X. Feng, Two-dimensional conjugated metal–organic frameworks (2D c -MOFs): chemistry and function for MOFtronics, Chem. Soc. Rev. 50 (4) (2021) 2764–2793, https://doi.org/10.1039/D0CS01160F.

[20] X. Zhuang, Y. Mai, D. Wu, F. Zhang, X. Feng, Two-dimensional soft nanomaterials: a fascinating world of materials, Adv. Mater. 27 (3) (2015) 403–427, https://doi.org/10.1002/adma.201401857.

[21] X. Chen, K. Geng, R. Liu, K.T. Tan, Y. Gong, Z. Li, S. Tao, Q. Jiang, D. Jiang, Covalent organic frameworks: chemical approaches to designer structures and built-in functions, Angew. Chem. Int. Ed. 59 (13) (2020) 5050–5091, https://doi.org/10.1002/anie.201904291.

[22] M. Ko, L. Mendecki, K.A. Mirica, Conductive two-dimensional metal-organic frameworks as multifunctional materials, Chem. Commun. 54 (57) (2018) 7873–7891, https://doi.org/10.1039/C8CC02871K.

[23] A.P. Côté, A.I. Benin, N.W. Ockwig, M. O'Keeffe, A.J. Matzger, O.M. Yaghi, Porous, crystalline, covalent organic frameworks, Science 310 (5751) (2005) 1166–1170, https://doi.org/10.1126/science.1120411.

[24] R.W. Day, D.K. Bediako, M. Rezaee, L.R. Parent, G. Skorupskii, M.Q. Arguilla, C.H. Hendon, I. Stassen, N.C. Gianneschi, P. Kim, M. Dincă, Single crystals of electrically conductive two-dimensional metal-organic frameworks:

[25] T. Chen, J.-H. Dou, L. Yang, C. Sun, N.J. Libretto, G. Skorupskii, J.T. Miller, M. Dincă, Continuous electrical conductivity variation in M 3 (hexaiminotriphenylene) 2 (M = Co, Ni, Cu) MOF alloys, J. Am. Chem. Soc. 142 (28) (2020) 12367–12373, https://doi.org/10.1021/jacs.0c04458.

[26] B. Hoppe, K.D.J. Hindricks, D.P. Warwas, H.A. Schulze, A. Mohmeyer, T.J. Pinkvos, S. Zailskas, M.R. Krey, C. Belke, S. König, M. Fröba, R.J. Haug, P. Behrens, Graphene-like metal-organic frameworks: morphology control, optimization of thin film electrical conductivity and fast sensing applications, CrystEngComm. 20 (41) (2018) 6458–6471, https://doi.org/10.1039/C8CE01264D.

[27] S.T. Yang, J. Kim, H.Y. Cho, S. Kim, W.S. Ahn, Facile synthesis of covalent organic frameworks COF-1 and COF-5 by sonochemical method, RSC Adv. 2 (2012) 10179–10181, https://doi.org/10.1039/c2ra21531d.

[28] B.J. Smith, W.R. Dichtel, Mechanistic studies of two-dimensional covalent organic frameworks rapidly polymerized from initially homogenous conditions, J. Am. Chem. Soc. 136 (24) (2014) 8783–8789, https://doi.org/10.1021/ja5037868.

[29] L. Mendecki, K.A. Mirica, Conductive metal-organic frameworks as ion-to-electron transducers in potentiometric sensors, ACS Appl. Mater. Interfaces. 10 (22) (2018) 19248–19257, https://doi.org/10.1021/acsami.8b03956.

[30] M. Ko, L. Mendecki, A.M. Eagleton, C.G. Durbin, R.M. Stolz, Z. Meng, K.A. Mirica, Employing conductive metal-organic frameworks for voltammetric detection of neurochemicals, J. Am. Chem. Soc. 142 (27) (2020) 11717–11733, https://doi.org/10.1021/jacs.9b13402.

[31] Y. Chen, H. Cui, J. Zhang, K. Zhao, D. Ding, J. Guo, L. Li, Z. Tian, Z. Tang, Surface growth of highly oriented covalent organic framework thin film with enhanced photoresponse speed, RSC Adv. 5 (112) (2015) 92573–92576, https://doi.org/10.1039/C5RA19430J.

[32] J. Guo, Y. Xu, S. Jin, L. Chen, T. Kaji, Y. Honsho, M.A. Addicoat, J. Kim, A. Saeki, H. Ihee, S. Seki, S. Irle, M. Hiramoto, J. Gao, D. Jiang, Conjugated organic framework with three-dimensionally ordered stable structure and delocalized π clouds, Nat. Commun. 4 (2013) 2736, https://doi.org/10.1038/ncomms3736.

[33] M. Ko, A. Aykanat, M.K. Smith, K.A. Mirica, Drawing sensors with ball-milled blends of metal-organic frameworks and graphite, Sensors 17 (2017) 2192, https://doi.org/10.3390/s17102192.

[34] J.W. Colson, W.R. Dichtel, Rationally synthesized two-dimensional polymers, Nat. Chem. 5 (6) (2013) 453–465, https://doi.org/10.1038/nchem.1628.

[35] D. Sheberla, L. Sun, M.A. Blood-Forsythe, S. Er, C.R. Wade, C.K. Brozek, A. Aspuru-Guzik, M. Dincă, High electrical conductivity in Ni3(2,3,6,7,10,11-hexaiminotriphenylene)2, a semiconducting metal-organic graphene analogue, J. Am. Chem. Soc. 136 (25) (2014) 8859–8862, https://doi.org/10.1021/ja502765n.

[36] M.K. Smith, K.A. Mirica, Self-organized frameworks on textiles (SOFT): conductive fabrics for simultaneous sensing, capture, and filtration of gases, J. Am. Chem. Soc. 139 (46) (2017) 16759–16767, https://doi.org/10.1021/jacs.7b08840.

[37] W.-H. Li, K. Ding, H.-R. Tian, M.-S. Yao, B. Nath, W.-H. Deng, Y. Wang, G. Xu, Conductive metal-organic framework nanowire array electrodes for high-performance solid-state supercapacitors, Adv. Funct. Mater. 27 (27) (2017) 1702067, https://doi.org/10.1002/adfm.201702067.

[38] M.K. Smith, K.E. Jensen, P.A. Pivak, K.A. Mirica, Direct self-assembly of conductive nanorods of metal-organic frameworks into chemiresistive devices on shrinkable polymer films, Chem. Mater. 28 (15) (2016) 5264–5268, https://doi.org/10.1021/acs.chemmater.6b02528.

[39] Y. Yue, S.-Y. Yang, Y.-L. Huang, B. Sun, S.-W. Bian, Reduced graphene oxide/polyester yarns supported conductive metal–organic framework nanorods as novel electrodes for all-solid-state supercapacitors, Energy Fuels 34 (12) (2020) 16879–16884, https://doi.org/10.1021/acs.energyfuels.0c03380.

[40] K. Zhou, C. Zhang, Z. Xiong, H.-Y. Chen, T. Li, G. Ding, B. Yang, Q. Liao, Y.e. Zhou, S.-T. Han, Template-directed growth of hierarchical MOF hybrid arrays for tactile sensor, Adv. Funct. Mater. 30 (38) (2020) 2001296, https://doi.org/10.1002/adfm.202001296.

[41] Y.-L. Li, J.-J. Zhou, M.-K. Wu, C. Chen, K. Tao, F.-Y. Yi, L. Han, Hierarchical Two-dimensional conductive metal-organic framework/layered double hydroxide nanoarray for a high-performance supercapacitor, Inorg. Chem. 57 (11) (2018) 6202–6205, https://doi.org/10.1021/acs.inorgchem.8b00493.

[42] A. Mähringer, M. Hennemann, T. Clark, T. Bein, D.D. Medina, Energy efficient ultrahigh flux separation of oily pollutants from water with superhydrophilic nanoscale metal-organic framework architectures, Angew. Chem. Int. Ed. 60 (10) (2021) 5519–5526, https://doi.org/10.1002/anie.202012428.

[43] J.W. Colson, A.R. Woll, A. Mukherjee, M.P. Levendorf, E.L. Spitler, V.B. Shields, M.G. Spencer, J. Park, W.R. Dichtel, Oriented 2D covalent organic framework thin films on single-layer graphene, Science 332 (6026) (2011) 228–231, https://doi.org/10.1126/science.1202747.

[44] JongTae Yoo, S.-J. Cho, G.Y. Jung, S.H. Kim, K.-H. Choi, J.-H. Kim, C.K. Lee, S.K. Kwak, S.-Y. Lee, COF-Net on CNT-Net as a molecularly designed, hierarchical porous chemical trap for polysulfides in lithium-sulfur batteries, Nano Lett. 16 (5) (2016) 3292–3300, https://doi.org/10.1021/acs.nanolett.6b00870.

[45] JongTae Yoo, SuHyun Lee, S. Hirata, ChaeRin Kim, C.K. Lee, T. Shiraki, N. Nakashima, J.K. Shim, In situ synthesis of covalent organic frameworks (COFs) on carbon nanotubes and graphenes by sonochemical reaction for CO2 adsorbents, Chem. Lett. 44 (4) (2015) 560–562, https://doi.org/10.1246/cl.141194.

[46] T. Bao, P. Tang, D. Kong, Z. Mao, Z. Chen, Polydopamine-supported immobilization of covalent-organic framework-5 in capillary as stationary phase for electrochromatographic separation, J. Chromatogr. A 1445 (2016) 140–148, https://doi.org/10.1016/j.chroma.2016.03.085.

[47] A.M. Evans, A. Giri, V.K. Sangwan, S. Xun, M. Bartnof, C.G. Torres-Castanedo, H. B. Balch, M.S. Rahn, N.P. Bradshaw, E. Vitaku, D.W. Burke, H. Li, M.J. Bedzyk, F. Wang, J.-L. Brédas, J.A. Malen, A.J.H. McGaughey, M.C. Hersam, W.R. Dichtel, P. E. Hopkins, Thermally conductive ultra-low-k dielectric layers based on two-dimensional covalent organic frameworks, Nat. Mater. 20 (8) (2021) 1142–1148, https://doi.org/10.1038/s41563-021-00934-3.

[48] D.D. Medina, V. Werner, F. Auras, R. Tautz, M. Dogru, J. Schuster, S. Linke, M. Döblinger, J. Feldmann, P. Knochel, T. Bein, Oriented thin films of a benzodithiophene covalent organic framework, ACS Nano 8 (4) (2014) 4042–4052, https://doi.org/10.1021/nn5000223.

[49] X. Song, S. Wang, Y. Li, C. Zheng, B. Zhang, C.-a. Di, F. Li, C. Jin, W. Mi, L. Chen, W. Hu, 2D semiconducting metal-organic framework thin films for organic spin valves, Angew. Chem. Int. Ed. 59 (3) (2020) 1118–1123, https://doi.org/10.1002/anie.v59.3.

[50] R. Li, S. Li, Q. Zhang, Y. Li, H. Wang, Layer-by-layer assembled triphenylene-based MOFs films for electrochromic electrode, Inorg. Chem. Commun. 123 (2021) 108354, https://doi.org/10.1016/j.inoche.2020.108354.

[51] M.-S. Yao, X.-J. Lv, Z.-H. Fu, W.-H. Li, W.-H. Deng, G.-D. Wu, G. Xu, Layer-by-layer assembled conductive metal-organic framework nanofilms for room-temperature chemiresistive sensing, Angew. Chem. Int. Ed. 56 (52) (2017) 16510–16514, https://doi.org/10.1002/anie.201709558.

[52] A. Mähringer, A.C. Jakowetz, J.M. Rotter, B.J. Bohn, J.K. Stolarczyk, J. Feldmann, T. Bein, D.D. Medina, Oriented thin films of electroactive triphenylene catecholate-based two-dimensional metal-organic frameworks, ACS Nano 13 (6) (2019) 6711–6719, https://doi.org/10.1021/acsnano.9b01137.

[53] D.D. Medina, J.M. Rotter, Y. Hu, M. Dogru, V. Werner, F. Auras, J.T. Markiewicz, P. Knochel, T. Bein, Room temperature synthesis of covalent-organic framework films through vapor-assisted conversion, J. Am. Chem. Soc. 137 (3) (2015) 1016–1019, https://doi.org/10.1021/ja510895m.

[54] V. Rubio-Giménez, M. Galbiati, J. Castells-Gil, N. Almora-Barrios, J. Navarro-Sánchez, G. Escorcia-Ariza, M. Mattera, T. Arnold, J. Rawle, S. Tatay, E. Coronado, C. Martí-Gastaldo, Bottom-up fabrication of semiconductive metal-organic framework ultrathin films, Adv. Mater. 30 (10) (2018) 1704291, https://doi.org/10.1002/adma.201704291.

[55] A.J. Clough, J.W. Yoo, M.H. Mecklenburg, S.C. Marinescu, Two-dimensional metal-organic surfaces for efficient hydrogen evolution from water, J. Am. Chem. Soc. 137 (1) (2015) 118–121, https://doi.org/10.1021/ja5116937.

[56] R. Dong, M. Pfeffermann, H. Liang, Z. Zheng, X. Zhu, J. Zhang, X. Feng, Large-area, free-standing, two-dimensional supramolecular polymer single-layer sheets for highly efficient electrocatalytic hydrogen evolution, Angew. Chem. Int. Ed. 54 (41) (2015) 12058–12063, https://doi.org/10.1002/anie.201506048.

[57] K. Yuan, T. Song, X. Zhu, B. Li, B. Han, L. Zheng, J. Li, X. Zhang, W. Hu, Construction of large-area ultrathin conductive metal-organic framework films through vapor-induced conversion, Small 15 (12) (2019) 1804845, https://doi.org/10.1002/smll.201804845.

[58] G. Wu, J. Huang, Y. Zang, J. He, G. Xu, Porous field-effect transistors based on a semiconductive metal-organic framework, J. Am. Chem. Soc. 139 (4) (2017) 1360–1363, https://doi.org/10.1021/jacs.6b08511.

[59] X.-L. Ye, Y.-Q. Huang, X.-Y. Tang, J. Xu, C. Peng, Y.-Z. Tan, Two-dimensional extended π-conjugated triphenylene-core covalent organic polymer, J. Mater. Chem. A 7 (7) (2019) 3066–3071, https://doi.org/10.1039/C8TA10554E.

[60] D.-G. Ha, M. Rezaee, Y. Han, S.A. Siddiqui, R.W. Day, L.S. Xie, B.J. Modtland, D. A. Muller, J. Kong, P. Kim, M. Dincă, M.A. Baldo, Large single crystals of two-dimensional π-conjugated metal-organic frameworks via biphasic solution-solid growth, ACS Cent. Sci. 7 (1) (2021) 104–109, https://doi.org/10.1021/acscentsci.0c01488.

[61] Y. Liu, Y. Wei, M. Liu, Y. Bai, X. Wang, S. Shang, C. Du, W. Gao, J. Chen, Y. Liu, Face-to-face growth of wafer-scale 2D semiconducting MOF films on dielectric substrates, Adv. Mater. 33 (13) (2021) 2007741, https://doi.org/10.1002/adma.202007741.

[62] R.P. Bisbey, C.R. DeBlase, B.J. Smith, W.R. Dichtel, Two-dimensional covalent organic framework thin films grown in flow, J. Am. Chem. Soc. 138 (36) (2016) 11433–11436, https://doi.org/10.1021/jacs.6b04669.

[63] N. Contreras-Pereda, D. Rodríguez-San-Miguel, C. Franco, S. Sevim, J.P. Vale, E. Solano, W.-K. Fong, A. Del Giudice, L. Galantini, R. Pfattner, S. Pané, T.S. Mayor, D. Ruiz-Molina, J. Puigmartí-Luis, Synthesis of 2D porous crystalline materials in simulated microgravity, Adv. Mater. 33 (30) (2021) 2101777, https://doi.org/10.1002/adma.202101777.

[64] S. Zint, D. Ebeling, S. Ahles, H.A. Wegner, A. Schirmeisen, Subsurface-controlled angular rotation: triphenylene molecules on Au(111) substrates, J. Phys. Chem. C 120 (3) (2016) 1615–1622, https://doi.org/10.1021/acs.jpcc.5b10602.

[65] L. Giovanelli, O. Ourdjini, M. Abel, R. Pawlak, J. Fujii, L. Porte, J.-M. Themlin, S. Clair, Combined photoemission spectroscopy and scanning tunneling microscopy study of the sequential dehydrogenation of hexahydroxytriphenylene on Ag(111), J. Phys. Chem. C 118 (27) (2014) 14899–14904, https://doi.org/10.1021/jp501849h.

[66] Z. Gao, C.-H. Hsu, J. Liu, F.-C. Chuang, R. Zhang, B. Xia, H.u. Xu, L.i. Huang, Q. Jin, P.N. Liu, N. Lin, Synthesis and characterization of a single-layer conjugated metal–organic structure featuring a non-trivial topological gap, Nanoscale 11 (3) (2019) 878–881, https://doi.org/10.1039/C8NR08477G.

[67] Z. Gao, Y. Gao, M. Hua, J. Liu, L.i. Huang, N. Lin, Design and synthesis of a single-layer ferromagnetic metal-organic framework with topological nontrivial gaps, J. Phys. Chem. C 124 (49) (2020) 27017–27023, https://doi.org/10.1021/acs.jpcc.0c08140.

[68] L. Yu, Z.-B. Li, D. Wang, Construction of boronate ester based single-layered covalent organic frameworks, Chem. Commun. 52 (95) (2016) 13771–13774, https://doi.org/10.1039/C6CC07399A.

[69] N.A.A. Zwaneveld, R. Pawlak, M. Abel, D. Catalin, D. Gigmes, D. Bertin, L. Porte, Organized formation of 2D extended covalent organic frameworks at surfaces, J. Am. Chem. Soc. 130 (21) (2008) 6678–6679, https://doi.org/10.1021/ja800906f.

[70] L. Sun, M.G. Campbell, M. Dincă, Electrically conductive porous metal-organic frameworks, Angew. Chem. Int. Ed. 55 (11) (2016) 3566–3579, https://doi.org/10.1002/anie.201506219.

[71] V. Rubio-Giménez, S. Tatay, C. Martí-Gastaldo, Electrical conductivity and magnetic bistability in metal–organic frameworks and coordination polymers: charge transport and spin crossover at the nanoscale, Chem. Soc. Rev. 49 (15) (2020) 5601–5638, https://doi.org/10.1039/C9CS00594C.

[72] M. Hmadeh, Z. Lu, Z. Liu, F. Gándara, H. Furukawa, S. Wan, V. Augustyn, R. Chang, L. Liao, F. Zhou, E. Perre, V. Ozolins, K. Suenaga, X. Duan, B. Dunn, Y. Yamamto, O. Terasaki, O.M. Yaghi, New porous crystals of extended metal-catecholates, Chem. Mater. 24 (18) (2012) 3511–3513, https://doi.org/10.1021/cm301194a.

[73] G. Skorupskii, B.A. Trump, T.W. Kasel, C.M. Brown, C.H. Hendon, M. Dincă, Efficient and tunable one-dimensional charge transport in layered lanthanide metal–organic frameworks, Nat. Chem. 12 (2) (2020) 131–136, https://doi.org/10.1038/s41557-019-0372-0.

[74] A. Mähringer, M. Döblinger, M. Hennemann, C. Gruber, D. Fehn, P.I. Scheurle, P. Hosseini, I. Santourian, A. Schirmacher, J.M. Rotter, G. Wittstock, K. Meyer, T. Clark, T. Bein, D.D. Medina, An electrically conducting three-dimensional iron-catecholate porous framework, Angew. Chem. Int. Ed. 60 (33) (2021) 18065–18072, https://doi.org/10.1002/anie.202102670.

[75] N.T.T. Nguyen, H. Furukawa, F. Gándara, C.A. Trickett, H.M. Jeong, K.E. Cordova, O.M. Yaghi, Three-dimensional metal-catecholate frameworks and their ultrahigh proton conductivity, J. Am. Chem. Soc. 137 (49) (2015) 15394–15397, https://doi.org/10.1021/jacs.5b10999.

[76] S. Zhou, X. Kong, B. Zheng, F. Huo, M. Strømme, C. Xu, Cellulose nanofiber @ conductive metal-organic frameworks for high-performance flexible supercapacitors, ACS Nano 13 (8) (2019) 9578–9586, https://doi.org/10.1021/acsnano.9b04670.

[77] E.M. Miner, L.u. Wang, M. Dincă, Modular O2 electroreduction activity in triphenylene-based metal-organic frameworks, Chem. Sci. 9 (29) (2018) 6286–6291, https://doi.org/10.1039/C8SC02049C.

[78] Y. Misumi, A. Yamaguchi, Z. Zhang, T. Matsushita, N. Wada, M. Tsuchiizu, K. Awaga, Quantum spin liquid state in a two-dimensional semiconductive metal−organic framework, J. Am. Chem. Soc. 142 (39) (2020) 16513–16517, https://doi.org/10.1021/jacs.0c05472.

[79] K.W. Nam, S.S. Park, R. dos Reis, V.P. Dravid, H. Kim, C.A. Mirkin, J.F. Stoddart, Conductive 2D metal-organic framework for high-performance cathodes in aqueous rechargeable zinc batteries, Nat. Commun. 10 (2019) 1–10, https://doi.org/10.1038/s41467-019-12857-4.

[80] M.E. Foster, K. Sohlberg, M.D. Allendorf, A.A. Talin, Unraveling the semiconducting/metallic discrepancy in Ni3(HITP)2, J. Phys. Chem. Lett. 9 (3) (2018) 481–486, https://doi.org/10.1021/acs.jpclett.7b03140.

[81] M.E. Foster, K. Sohlberg, C.D. Spataru, M.D. Allendorf, Proposed modification of the graphene analogue Ni3(HITP)2 to yield a semiconducting material, J. Phys. Chem. C 120 (27) (2016) 15001–15008, https://doi.org/10.1021/acs.jpcc.6b05746.

[82] M.G. Campbell, D. Sheberla, S.F. Liu, T.M. Swager, M. Dincă, Cu 3 (hexaiminotriphenylene) 2: an electrically conductive 2D metal-organic framework for chemiresistive sensing, Angew. Chem. Int. Ed. 54 (2015) 4349–4352, https://doi.org/10.1002/anie.201411854.

[83] S. Chen, J. Dai, X.C. Zeng, Metal-organic kagome lattices M3(2,3,6,7,10,11-hexaiminotriphenylene)2 (M = Ni and Cu): from semiconducting to metallic by metal substitution, Phys. Chem. Chem. Phys. 17 (8) (2015) 5954–5958, https://doi.org/10.1039/C4CP05328A.

[84] R. Iqbal, M.Q. Sultan, M. Hussain, M. Hamza, A. Tariq, M.B. Akbar, Y. Ma, L. Zhi, The different roles of cobalt and manganese in metal-organic frameworks for supercapacitors, Adv. Mater. Technol. 6 (3) (2021) 2000941, https://doi.org/10.1002/admt.202000941.

[85] Y. Zang, F. Pei, J. Huang, Z. Fu, G. Xu, X. Fang, Large-area preparation of crack-free crystalline microporous conductive membrane to upgrade high energy lithium-sulfur batteries, Adv. Energy Mater. 8 (31) (2018) 1802052, https://doi.org/10.1002/aenm.201802052.

[86] D. Sheberla, J.C. Bachman, J.S. Elias, C.-J. Sun, Y. Shao-Horn, M. Dincă, Conductive MOF electrodes for stable supercapacitors with high areal capacitance, Nat. Mater. 16 (2) (2017) 220–224, https://doi.org/10.1038/nmat4766.

[87] L. Sun, B. Liao, D. Sheberla, D. Kraemer, J. Zhou, E.A. Stach, D. Zakharov, V. Stavila, A.A. Talin, Y. Ge, M.D. Allendorf, G. Chen, F. Léonard, M. Dincă, A microporous and naturally nanostructured thermoelectric metal-organic framework with ultralow thermal conductivity, Joule 1 (1) (2017) 168–177, https://doi.org/10.1016/j.joule.2017.07.018.

[88] Y. Lian, W. Yang, C. Zhang, H. Sun, Z. Deng, W. Xu, L.i. Song, Z. Ouyang, Z. Wang, J. Guo, Y. Peng, Unpaired 3d electrons on atomically dispersed cobalt centres in coordination polymers regulate both oxygen reduction reaction

(ORR) activity and selectivity for use in zinc-air batteries, Angew. Chem. Int. Ed. 59 (1) (2020) 286–294, https://doi.org/10.1002/anie.201910879.

[89] Y. Nonoguchi, D. Sato, T. Kawai, Crystallinity-dependent thermoelectric properties of a two-dimensional coordination polymer: Ni3(2,3,6,7,10,11-hexaiminotriphenylene)2, Polymers 10 (2018) 962, https://doi.org/10.3390/polym10090962.

[90] J. Cui, Z. Xu, An electroactive porous network from covalent metal–dithiolene links, Chem. Commun. 50 (30) (2014) 3986–3988, https://doi.org/10.1039/C4CC00408F.

[91] A.J. Clough, J.M. Skelton, C.A. Downes, A.A. de la Rosa, J.W. Yoo, A. Walsh, B.C. Melot, S.C. Marinescu, Metallic conductivity in a two-dimensional cobalt dithiolene metal-organic framework, J. Am. Chem. Soc. 139 (31) (2017) 10863–10867, https://doi.org/10.1021/jacs.7b05742.

[92] R. Dong, P. Han, H. Arora, M. Ballabio, M. Karakus, Z. Zhang, C. Shekhar, P. Adler, P.S. Petkov, A. Erbe, S.C.B. Mannsfeld, C. Felser, T. Heine, M. Bonn, X. Feng, E. Cánovas, High-mobility band-like charge transport in a semiconducting two-dimensional metal–organic framework, Nat. Mater. 17 (11) (2018) 1027–1032, https://doi.org/10.1038/s41563-018-0189-z.

[93] L. Mendecki, M. Ko, X. Zhang, Z. Meng, K.A. Mirica, Porous scaffolds for electrochemically controlled reversible capture and release of ethylene, J. Am. Chem. Soc. 139 (48) (2017) 17229–17232, https://doi.org/10.1021/jacs.7b08102.

[94] A.J. Clough, N.M. Orchanian, J.M. Skelton, A.J. Neer, S.A. Howard, C.A. Downes, L.F.J. Piper, A. Walsh, B.C. Melot, S.C. Marinescu, Room temperature metallic conductivity in a metal-organic framework induced by oxidation, J. Am. Chem. Soc. 141 (41) (2019) 16323–16330, https://doi.org/10.1021/jacs.9b06898.

[95] Q. Zhou, J. Wang, T.S. Chwee, G. Wu, X. Wang, Q. Ye, J. Xu, S.-W. Yang, Topological insulators based on 2D shape-persistent organic ligand complexes, Nanoscale 7 (2) (2015) 727–735, https://doi.org/10.1039/C4NR05247A.

[96] Y. He, C.D. Spataru, F. Léonard, R.E. Jones, M.E. Foster, M.D. Allendorf, A. Alec Talin, Two-dimensional metal-organic frameworks with high thermoelectric efficiency through metal ion selection, Phys. Chem. Chem. Phys. 19 (29) (2017) 19461–19467, https://doi.org/10.1039/C7CP03310A.

[97] R. Dong, Z. Zhang, D.C. Tranca, J. Zhang, N. Chandrasekhar, S. Liu, X. Zhuang, G. Seifert, X. Feng, Immobilizing molecular metal dithiolene-diamine complexes on 2D metal-organic frameworks for electrocatalytic H 2 production, Chem. Eur. J. 23 (10) (2017) 2255–2260, https://doi.org/10.1002/chem.201605337.

[98] M.-S. Yao, J.-J. Zheng, A.-Q. Wu, G. Xu, S.S. Nagarkar, G. Zhang, M. Tsujimoto, S. Sakaki, S. Horike, K. Otake, S. Kitagawa, A dual-ligand porous coordination polymer chemiresistor with modulated conductivity and porosity, Angew. Chem. Int. Ed. 59 (1) (2020) 172–176, https://doi.org/10.1002/anie.201909096.

[99] Y. Cui, J. Yan, Z. Chen, W. Xing, C. Ye, X. Li, Y.e. Zou, Y. Sun, C. Liu, W. Xu, D. Zhu, Synthetic route to a triphenylenehexaselenol-based metal organic framework with semi-conductive and glassy magnetic properties, IScience 23 (1) (2020) 100812, https://doi.org/10.1016/j.isci.2019.100812.

[100] V. Rubio-Giménez, N. Almora-Barrios, G. Escorcia-Ariza, M. Galbiati, M. Sessolo, S. Tatay, C. Martí-Gastaldo, Origin of the chemiresistive response of ultrathin films of conductive metal-organic frameworks, Angew. Chem. Int. Ed. 57 (46) (2018) 15086–15090, https://doi.org/10.1002/anie.201808242.

[101] R.M. Stolz, A. Mahdavi-Shakib, B.G. Frederick, K.A. Mirica, Host-guest interactions and redox activity in layered conductive metal-organic frameworks, Chem. Mater. 32 (18) (2020) 7639–7652, https://doi.org/10.1021/acs.chemmater.0c01007.

[102] M.G. Campbell, S.F. Liu, T.M. Swager, M. Dincă, Chemiresistive sensor arrays from conductive 2D metal-organic frameworks, J. Am. Chem. Soc. 137 (43) (2015) 13780–13783, https://doi.org/10.1021/jacs.5b09600.

[103] H. Wu, W. Zhang, S. Kandambeth, O. Shekhah, M. Eddaoudi, H.N. Alshareef, Conductive metal-organic frameworks selectively grown on laser-scribed graphene for electrochemical microsupercapacitors, Adv. Energy Mater. 9 (21) (2019) 1900482, https://doi.org/10.1002/aenm.201900482.

[104] E.M. Miner, T. Fukushima, D. Sheberla, L. Sun, Y. Surendranath, M. Dincă, Electrochemical oxygen reduction catalysed by Ni3(hexaiminotriphenylene) 2, Nat. Commun. 7 (2016) 10942, https://doi.org/10.1038/ncomms10942.

[105] Y.u. Tian, Z. Zhang, C. Wu, L. Yan, W. Chen, Z. Su, Theoretical insights into the catalytic mechanism for the oxygen reduction reaction on M3 (hexaiminotriphenylene)2 (M = Ni, Cu), Phys. Chem. Chem. Phys. 20 (3) (2018) 1821–1828, https://doi.org/10.1039/C7CP02052J.

[106] W.-H. Li, J. Lv, Q. Li, J. Xie, N. Ogiwara, Y. Huang, H. Jiang, H. Kitagawa, G. Xu, Y. Wang, Conductive metal-organic framework nanowire arrays for electrocatalytic oxygen evolution, J. Mater. Chem. A 7 (17) (2019) 10431–10438, https://doi.org/10.1039/C9TA02169H.

[107] Y. Tian, Y. Wang, L. Yan, J. Zhao, Z. Su, Electrochemical reduction of carbon dioxide on the two–dimensional M3(Hexaiminotriphenylene)2 sheet: a computational study, Appl. Surf. Sci. 467–468 (2019) 98–103, https://doi.org/10.1016/j.apsusc.2018.10.131.

[108] W. Zhu, C. Zhang, Q. Li, L. Xiong, R. Chen, X. Wan, Z. Wang, W. Chen, Z. Deng, Y. Peng, Selective reduction of CO2 by conductive MOF nanosheets as an efficient co-catalyst under visible light illumination, Appl. Catal. B Environ. 238 (2018) 339–345, https://doi.org/10.1016/j.apcatb.2018.07.024.

[109] L. Yang, X. He, M. Dincă, Triphenylene-Bridged trinuclear complexes of Cu: models for spin interactions in two-dimensional electrically conductive metal-organic frameworks, J. Am. Chem. Soc. 141 (26) (2019) 10475–10480, https://doi.org/10.1021/jacs.9b04822.

[110] L. Yang, M. Dincă, Redox ladder of Ni3 complexes with closed-shell, mono-, and diradical triphenylene units: molecular models for conductive 2D MOFs, Angew. Chem. Int. Ed. 60 (44) (2021) 23784–23789, https://doi.org/10.1002/anie.202109304.

[111] Y. Sun, H. Li, X. Gao, Z. Yu, Z. Huang, C. Zhang, Superb nonlinear absorption of triphenylene-based metal-organic frameworks associated with abundant metal d electrons, Adv. Opt. Mater. 9 (17) (2021) 2100622, https://doi.org/10.1002/adom.202100622.

[112] H. Arora, R. Dong, T. Venanzi, J. Zscharschuch, H. Schneider, M. Helm, X. Feng, E. Cánovas, A. Erbe, Demonstration of a broadband photodetector based on a two-dimensional metal-organic framework, Adv. Mater. 32 (9) (2020) 1907063, https://doi.org/10.1002/adma.201907063.

[113] A.P. Côté, H.M. El-Kaderi, H. Furukawa, J.R. Hunt, O.M. Yaghi, Reticular synthesis of microporous and mesoporous 2D covalent organic frameworks, J. Am. Chem. Soc. 129 (43) (2007) 12914–12915, https://doi.org/10.1021/ja0751781.

[114] H. Furukawa, O.M. Yaghi, Storage of hydrogen, methane, and carbon dioxide in highly porous covalent organic frameworks for clean energy applications, J. Am. Chem. Soc. 131 (25) (2009) 8875–8883, https://doi.org/10.1021/ja9015765.

[115] X. Chen, M. Addicoat, E. Jin, H. Xu, T. Hayashi, F. Xu, N. Huang, S. Irle, D. Jiang, Designed synthesis of double-stage two-dimensional covalent organic frameworks, Sci. Rep. 5 (2015) 14650, https://doi.org/10.1038/srep14650.

[116] Y. Zeng, R. Zou, Z. Luo, H. Zhang, X. Yao, X. Ma, R. Zou, Y. Zhao, Covalent organic frameworks formed with two types of covalent bonds based on orthogonal reactions, J. Am. Chem. Soc. 137 (3) (2015) 1020–1023, https://doi.org/10.1021/ja510926w.

[117] X. Guan, H. Li, Y. Ma, M. Xue, Q. Fang, Y. Yan, V. Valtchev, S. Qiu, Chemically stable polyarylether-based covalent organic frameworks, Nat. Chem. 11 (6) (2019) 587–594, https://doi.org/10.1038/s41557-019-0238-5.

[118] B. Zhang, M. Wei, H. Mao, X. Pei, S.A. Alshmimri, J.A. Reimer, O.M. Yaghi, Crystalline dioxin-linked covalent organic frameworks from irreversible reactions, J. Am. Chem. Soc. 140 (40) (2018) 12715–12719, https://doi.org/10.1021/jacs.8b08374.

[119] W. Ji, Y.-S. Guo, H.-M. Xie, X. Wang, X. Jiang, D.-S. Guo, Rapid microwave synthesis of dioxin-linked covalent organic framework for efficient micro-extraction of perfluorinated alkyl substances from water, J. Hazard. Mater. 397 (2020) 122793, https://doi.org/10.1016/j.jhazmat.2020.122793.

[120] G.H.V. Bertrand, V.K. Michaelis, T.-C. Ong, R.G. Griffin, M. Dinca, Thiophene-based covalent organic frameworks, Proc. Natl. Acad. Sci. U.S.A. 110 (13) (2013) 4923–4928, https://doi.org/10.1073/pnas.1221824110.

[121] X. Feng, L. Chen, Y. Honsho, O. Saengsawang, L. Liu, Lu. Wang, A. Saeki, S. Irle, S. Seki, Y. Dong, D. Jiang, An ambipolar conducting covalent organic framework with self-sorted and periodic electron donor-acceptor ordering, Adv. Mater. 24 (22) (2012) 3026–3031, https://doi.org/10.1002/adma.201201185.

[122] S.S. Han, H. Furukawa, O.M. Yaghi, W.A. Goddard, Covalent organic frameworks as exceptional hydrogen storage materials, J. Am. Chem. Soc. 130 (35) (2008) 11580–11581, https://doi.org/10.1021/ja803247y.

[123] H. Yang, Y.a. Du, S. Wan, G.D. Trahan, Y. Jin, W. Zhang, Mesoporous 2D covalent organic frameworks based on shape-persistent arylene-ethynylene macrocycles, Chem. Sci. 6 (7) (2015) 4049–4053, https://doi.org/10.1039/C5SC00894H.

[124] A. Nagai, Z. Guo, X. Feng, S. Jin, X. Chen, X. Ding, D. Jiang, Pore surface engineering in covalent organic frameworks, Nat. Commun. 2 (2011) 536, https://doi.org/10.1038/ncomms1542.

[125] E.L. Spitler, M.R. Giovino, S.L. White, W.R. Dichtel, A mechanistic study of Lewis acid-catalyzed covalent organic framework formation, Chem. Sci. 2 (8) (2011) 1588–1593, https://doi.org/10.1039/C1SC00260K.

[126] B.J. Smith, N. Hwang, A.D. Chavez, J.L. Novotney, W.R. Dichtel, Growth rates and water stability of 2D boronate ester covalent organic frameworks, Chem. Commun. 51 (35) (2015) 7532–7535, https://doi.org/10.1039/C5CC00379B.

[127] D.A. Vazquez-Molina, G.S. Mohammad-Pour, C. Lee, M.W. Logan, X. Duan, J.K. Harper, F.J. Uribe-Romo, Mechanically shaped two-dimensional covalent organic frameworks reveal crystallographic alignment and fast Li-Ion conductivity, J. Am. Chem. Soc. 138 (31) (2016) 9767–9770, https://doi.org/10.1021/jacs.6b05568.

[128] N.L. Campbell, R. Clowes, L.K. Ritchie, A.I. Cooper, Rapid Microwave synthesis and purification of porous covalent organic frameworks, Chem. Mater. 21 (2) (2009) 204–206, https://doi.org/10.1021/cm802981m.

[129] M. Calik, T. Sick, M. Dogru, M. Döblinger, S. Datz, H. Budde, A. Hartschuh, F. Auras, T. Bein, From highly crystalline to outer surface-functionalized covalent organic frameworks-a modulation approach, J. Am. Chem. Soc. 138 (4) (2016) 1234–1239, https://doi.org/10.1021/jacs.5b10708.

[130] Y.-B. Huang, P. Pachfule, J.-K. Sun, Q. Xu, From covalent-organic frameworks to hierarchically porous B-doped carbons: a molten-salt approach, J. Mater. Chem. A 4 (11) (2016) 4273–4279, https://doi.org/10.1039/C5TA10170K.

[131] Y. Du, K. Mao, P. Kamakoti, B. Wooler, S. Cundy, Q. Li, P. Ravikovitch, D. Calabro, The effects of pyridine on the structure of B-COFs and the underlying mechanism, J. Mater. Chem. A 1 (2013) 13171–13178, https://doi.org/10.1039/c3ta12515g.

[132] B.J. Smith, L.R. Parent, A.C. Overholts, P.A. Beaucage, R.P. Bisbey, A.D. Chavez, N. Hwang, C. Park, A.M. Evans, N.C. Gianneschi, W.R. Dichtel, Colloidal covalent organic frameworks, ACS Cent. Sci. 3 (1) (2017) 58–65, https://doi.org/10.1021/acscentsci.6b00331.

[133] C.J. Doonan, D.J. Tranchemontagne, T.G. Glover, J.R. Hunt, O.M. Yaghi, Exceptional ammonia uptake by a covalent organic framework, Nat. Chem. 2 (3) (2010) 235–238, https://doi.org/10.1038/nchem.548.

[134] I. Berlanga, M.L. Ruiz-González, J.M. González-Calbet, J.L.G. Fierro, R. Mas-Ballesté, F. Zamora, Delamination of layered covalent organic frameworks, Small 7 (9) (2011) 1207–1211, https://doi.org/10.1002/smll.201002264.

[135] S. Wan, J. Guo, J. Kim, H. Ihee, D. Jiang, A Belt-Shaped, Blue luminescent, and semiconducting covalent organic framework, Angew. Chem. Int. Ed. 47 (2008) 8826–8830, https://doi.org/10.1002/anie.200803826.

[136] M.S. Lohse, J.M. Rotter, J.T. Margraf, V. Werner, M. Becker, S. Herbert, P. Knochel, T. Clark, T. Bein, D.D. Medina, From benzodithiophene to diethoxy-benzodithiophene covalent organic frameworks-structural investigations, CrystEngComm 18 (23) (2016) 4295–4302, https://doi.org/10.1039/C6CE00193A.

[137] S. Duhović, M. Dincă, Synthesis and electrical properties of covalent organic frameworks with heavy chalcogens, Chem. Mater. 27 (16) (2015) 5487–5490, https://doi.org/10.1021/acs.chemmater.5b02358.

[138] M. Dogru, M. Handloser, F. Auras, T. Kunz, D. Medina, A. Hartschuh, P. Knochel, T. Bein, A photoconductive thienothiophene-based covalent organic framework showing charge transfer towards included fullerene, Angew. Chem. Int. Ed. 52 (10) (2013) 2920–2924, https://doi.org/10.1002/anie.201208514.

[139] D.D. Medina, M.L. Petrus, A.N. Jumabekov, J.T. Margraf, S. Weinberger, J.M. Rotter, T. Clark, T. Bein, Directional charge-carrier transport in oriented benzodithiophene covalent organic framework thin films, ACS Nano 11 (3) (2017) 2706–2713, https://doi.org/10.1021/acsnano.6b07692.

[140] E.L. Spitler, B.T. Koo, J.L. Novotney, J.W. Colson, F.J. Uribe-Romo, G.D. Gutierrez, P. Clancy, W.R. Dichtel, A 2D covalent organic framework with 4.7-nm pores and insight into its interlayer stacking, J. Am. Chem. Soc. 133 (2011) 19416–19421, https://doi.org/10.1021/ja206242v.

[141] Jian Zhang, Laibing Wang, Na Li, Jiangfei Liu, Wei Zhang, Zhengbiao Zhang, Nianchen Zhou, Xiulin Zhu, A novel azobenzene covalent organic framework, CrystEngComm 16 (29) (2014) 6547–6551, https://doi.org/10.1039/C4CE00369A.

[142] Chunhua Liu, Yanxia Yu, Wei Zhang, Qingdao Zeng, Shengbin Lei, Room-temperature synthesis of covalent organic frameworks with a boronic ester linkage at the liquid/solid interface, Chem. Eur. J. 22 (51) (2016) 18412–18418, https://doi.org/10.1002/chem.201603547.

[143] Laura M. Salonen, Dana D. Medina, Enrique Carbó-Argibay, Maarten G. Goesten, Luís Mafra, Noelia Guldris, Julian M. Rotter, Daniel G. Stroppa, Carlos Rodríguez-Abreu, A supramolecular strategy based on molecular dipole moments for high-quality covalent organic frameworks, Chem. Commun. 52 (51) (2016) 7986–7989, https://doi.org/10.1039/C6CC02170K.

[144] F. Xu, S. Jin, H. Zhong, D. Wu, X. Yang, X. Chen, H. Wei, R. Fu, D. Jiang, Electrochemically active, crystalline, mesoporous covalent organic frameworks on carbon nanotubes for synergistic lithium-ion battery energy storage, Sci. Rep. 5 (2015) 8225, https://doi.org/10.1038/srep08225.

[145] S. Jin, K. Furukawa, M. Addicoat, L. Chen, S. Takahashi, S. Irle, T. Nakamura, D. Jiang, Large pore donor—acceptor covalent organic frameworks, Chem. Sci. 4 (2013) 4505–4511, https://doi.org/10.1039/c3sc52034j.

[146] Sabrina Rager, Mirjam Dogru, Veronika Werner, Andrej Gavryushin, Maria Götz, Hanna Engelke, Dana D. Medina, Paul Knochel, Thomas Bein, Pore wall fluorescence labeling of covalent organic frameworks, CrystEngComm 19 (33) (2017) 4886–4891, https://doi.org/10.1039/C7CE00684E.

[147] Mona Calik, Florian Auras, Laura M. Salonen, Kathrin Bader, Irene Grill, Matthias Handloser, Dana D. Medina, Mirjam Dogru, Florian Löbermann, Dirk Trauner, Achim Hartschuh, Thomas Bein, Extraction of photogenerated electrons and holes from a covalent organic framework integrated heterojunction, J. Am. Chem. Soc. 136 (51) (2014) 17802–17807, https://doi.org/10.1021/ja509551m.

[148] N. Huang, L. Zhai, D.E. Coupry, M.A. Addicoat, K. Okushita, K. Nishimura, T. Heine, D. Jiang, Multiple-component covalent organic frameworks, Nat. Commun. 7 (2016) 12325, https://doi.org/10.1038/ncomms12325.

[149] Zheng Meng, Aylin Aykanat, Katherine A. Mirica, Proton conduction in 2D aza-fused covalent organic frameworks, Chem. Mater. 31 (3) (2019) 819–825, https://doi.org/10.1021/acs.chemmater.8b03897.

[150] I. Ahmad, F. Li, C. Kim, J.-M. Seo, G. Kim, J. Mahmood, H.Y. Jeong, J.-B. Baek, Robust fused aromatic pyrazine-based two-dimensional network for stably cocooning iron nanoparticles as an oxygen reduction electrocatalyst, Nano Energy 56 (2019) 581–587, https://doi.org/10.1016/j.nanoen.2018.12.007.

[151] Yunchao Ma, Xiaozhou Liu, Xinyu Guan, Hui Li, Yusran Yusran, Ming Xue, Qianrong Fang, Yushan Yan, Shilun Qiu, Valentin Valtchev, One-pot cascade syntheses of microporous and mesoporous pyrazine-linked covalent organic frameworks as Lewis-acid catalysts, Dalton Trans. 48 (21) (2019) 7352–7357, https://doi.org/10.1039/C8DT05056B.

[152] Samik Jhulki, Jeehong Kim, In-Chul Hwang, Golam Haider, Jiyong Park, Ji Young Park, Yeonsang Lee, Wooseup Hwang, Ajaz Ahmed Dar, Barun Dhara, Sang Hoon Lee, Juho Kim, Jin Young Koo, Moon Ho Jo, Chan-Cuk Hwang, Young Hwa Jung, Youngsin Park, Monika Kataria, Yang-Fang Chen, Seung-Hoon Jhi, Mu-Hyun Baik, Kangkyun Baek, Kimoon Kim, Solution-Processable, Crystalline π-Conjugated Two-Dimensional Polymers with High Charge Carrier Mobility, Chemistry 6 (8) (2020) 2035–2045, https://doi.org/10.1016/j.chempr.2020.05.026.

[153] R. Zhou, Y. Huang, Z. Li, S. Kang, X. Wang, S. Liu, Piperazine-based two-dimensional covalent organic framework for high performance anodic lithium storage, Energy Storage Mater. 40 (2021) 124–138, https://doi.org/10.1016/j.ensm.2021.05.008.

[154] Ryota Matsuoka, Ryojun Toyoda, Ryo Shiotsuki, Naoya Fukui, Keisuke Wada, Hiroaki Maeda, Ryota Sakamoto, Sono Sasaki, Hiroyasu Masunaga, Kosuke Nagashio, Hiroshi Nishihara, Expansion of the graphdiyne family: a triphenylene-cored analogue, ACS Appl. Mater. Interfaces. 11 (3) (2019) 2730–2733, https://doi.org/10.1021/acsami.8b00743.

[155] Shan Wang, Li Ma, Qianyou Wang, Pengpeng Shao, Dou Ma, Shuai Yuan, Peng Lei, Pengfei Li, Xiao Feng, Bo Wang, Covalent organic frameworks: a platform for the experimental establishment of the influence of intermolecular distance on phosphorescence, J. Mater. Chem. C 6 (20) (2018) 5369–5374, https://doi.org/10.1039/C8TC01559G.

[156] Austin M. Evans, Lucas R. Parent, Nathan C. Flanders, Ryan P. Bisbey, Edon Vitaku, Matthew S. Kirschner, Richard D. Schaller, Lin X. Chen, Nathan C. Gianneschi, William R. Dichtel, Seeded growth of single-crystal two-dimensional covalent organic frameworks, Science 361 (6397) (2018) 52–57, https://doi.org/10.1126/science.aar7883.

[157] Nathan C. Flanders, Matthew S. Kirschner, Pyosang Kim, Thomas J. Fauvell, Austin M. Evans, Waleed Helweh, Austin P. Spencer, Richard D. Schaller, William R. Dichtel, Lin X. Chen, Large exciton diffusion coefficients in two-dimensional covalent organic frameworks with different domain sizes revealed by ultrafast exciton dynamics, J. Am. Chem. Soc. 142 (35) (2020) 14957–14965, https://doi.org/10.1021/jacs.0c05404.

[158] Lingkun Meng, Siyuan Ren, Chenhui Ma, Ying Yu, Yue Lou, Dong Zhang, Zhan Shi, Synthesis of a 2D nitrogen-rich π-conjugated microporous polymer for high performance lithium-ion batteries, Chem. Commun. 55 (64) (2019) 9491–9494, https://doi.org/10.1039/C9CC04036F.

[159] Zhenbin Guo, Yuanyuan Zhang, Yu Dong, Jie Li, Siwu Li, Pengpeng Shao, Xiao Feng, Bo Wang, Fast ion transport pathway provided by polyethylene glycol confined in covalent organic frameworks, J. Am. Chem. Soc. 141 (5) (2019) 1923–1927, https://doi.org/10.1021/jacs.8b13551.

[160] Chunhua Yang, Zhao-Di Yang, Hong Dong, Ning Sun, Yang Lu, Feng-Ming Zhang, Guiling Zhang, Theory-driven design and targeting synthesis of a highly-conjugated basal-plane 2D covalent organic framework for metal-free electrocatalytic OER, ACS Energy Lett. 4 (9) (2019) 2251–2258, https://doi.org/10.1021/acsenergylett.9b01691.

[161] Jin-Hu Dou, Maxx Q. Arguilla, Yi Luo, Jian Li, Weizhe Zhang, Lei Sun, Jenna L. Mancuso, Luming Yang, Tianyang Chen, Lucas R. Parent, Grigorii Skorupskii, Nicole J. Libretto, Chenyue Sun, Min Chieh Yang, Phat Vinh Dip, Edward J. Brignole, Jeffrey T. Miller, Jing Kong, Christopher H. Hendon, Junliang Sun, Mircea Dincă, Atomically precise single-crystal structures of electrically conducting 2D metal–organic frameworks, Nat. Mater. 20 (2) (2021) 222–228, https://doi.org/10.1038/s41563-020-00847-7.

[162] Renhao Dong, Xinliang Feng, Making large single crystals of 2D MOFs, Nat. Mater. 20 (2) (2021) 122–123, https://doi.org/10.1038/s41563-020-00912-1.

[163] Minghao Yu, Renhao Dong, Xinliang Feng, Two-dimensional carbon-rich conjugated frameworks for electrochemical energy applications, J. Am. Chem. Soc. 142 (30) (2020) 12903–12915, https://doi.org/10.1021/jacs.0c05130.

[164] Zheng Meng, Katherine A. Mirica, Two-dimensional d-π conjugated metal-organic framework based on hexahydroxytrinaphthylene, Nano Res. 14 (2) (2021) 369–375, https://doi.org/10.1007/s12274-020-2874-x.

[165] Hua Zhang, Ultrathin two-dimensional nanomaterials, ACS Nano 9 (10) (2015) 9451–9469, https://doi.org/10.1021/acsnano.5b05040.

[166] N. Contreras-Pereda, P. Hayati, S. Suárez-García, L. Esrafili, P. Retailleau, S. Benmansour, F. Novio, A. Morsali, D. Ruiz-Molina, Delamination of 2D coordination polymers: the role of solvent and ultrasound, Ultrason. Sonochem. 55 (2019) 186–195, https://doi.org/10.1016/j.ultsonch.2019.02.014.

[167] Noemí Contreras-Pereda, Faezeh Moghzi, Javier Baselga, Haixia Zhong, Jan Janczak, Janet Soleimannejad, Renhao Dong, Daniel Ruiz-Molina, Ultrasound-assisted exfoliation of a layered 2D coordination polymer with HER electrocatalytic activity, Ultrason. Sonochem. 70 (2021) 105292, https://doi.org/10.1016/j.ultsonch.2020.105292.

[168] Belén Pepió, Noemí Contreras-Pereda, Salvio Suárez-García, Payam Hayati, Samia Benmansour, Pascal Retailleau, Ali Morsali, Daniel Ruiz-Molina, Solvent-tuned ultrasonic synthesis of 2D coordination polymer nanostructures and flakes, Ultrason. Sonochem. 72 (2021) 105425, https://doi.org/10.1016/j.ultsonch.2020.105425.

[169] Matthias Lischka, Renhao Dong, Mingchao Wang, Natalia Martsinovich, Massimo Fritton, Lukas Grossmann, Wolfgang M. Heckl, Xinliang Feng, Markus Lackinger, Competitive metal coordination of hexaaminotriphenylene on Cu(111) by intrinsic copper versus extrinsic nickel adatoms, Chem. Eur. J. 25 (8) (2019) 1975–1983, https://doi.org/10.1002/chem.201803908.